The Astrophysical Journal, 944:200 (22pp), 2023 February 20 https://doi.org/10.3847/1538-4357/acb13e

Photometric Objects Around Cosmic Webs (PAC) Delineated in a Spectroscopic Survey. IV. High-precision Constraints on the Evolution of the Stellar–Halo Mass Relation at Redshift $z < 0.7$

Kun Xu[1], Y. P. Jing[1,2], Yun Zheng[1], and Hongyu Gao[1]
[1] Department of Astronomy, School of Physics and Astronomy, Shanghai Jiao Tong University, Shanghai, 200240, People's Republic of China; ypjing@sjtu.edu.cn
[2] Tsung-Dao Lee Institute, and Shanghai Key Laboratory for Particle Physics and Cosmology, Shanghai Jiao Tong University, Shanghai, 200240, People's Republic of China
Received 2022 November 4; revised 2023 January 4; accepted 2023 January 5; published 2023 February 27

Abstract

Taking advantage of the Photometric objects Around Cosmic webs method developed in Paper I, we measure the excess surface density $\bar{n}_2 w_p$ of the photometric objects around spectroscopic objects down to stellar masses $10^{8.0}M_\odot$, $10^{9.2}M_\odot$, and $10^{9.8}M_\odot$ in the redshift ranges of $z_s < 0.2$, $0.2 < z_s < 0.4$, and $0.5 < z_s < 0.7$, respectively, using data from the DESI Legacy Imaging Surveys and spectroscopic samples from the Sloan Digital Sky Survey (i.e., the Main, LOWZ, and CMASS samples). We model the measured $\bar{n}_2 w_p$ in an N-body simulation, using the abundance matching method, and we constrain the stellar–halo mass relations (SHMRs) in the three redshift ranges to percent levels. With the accurate modeling, we demonstrate that the stellar mass scatter for a given halo mass is nearly a constant, and that the empirical form of Behroozi et al. describes the SHMR better than the double-power-law form at low mass. Our SHMR accurately captures the downsizing of massive galaxies from $z_s = 0.7$, while it also indicates that small galaxies are still growing faster than their host halos. The galaxy stellar mass functions (GSMFs) from our modeling are in perfect agreement with the model-independent measurements in Paper III, although the current work extends the GSMFs to a much smaller stellar mass. Based on the GSMFs and the SHMRs, we derive the stellar mass completeness and halo occupation distributions for the LOWZ and CMASS samples, which are useful for correctly interpreting their cosmological measurements, such as galaxy–galaxy lensing and redshift space distortion.

Unified Astronomy Thesaurus concepts: Galaxy abundances (574); Galaxy formation (595); Galaxy properties (615); Galaxy dark matter halos (1880)

1. Introduction

With the rapid developments in cosmology, we have entered an era of understanding galaxy formation in the cosmological framework (Mo et al. 2010; Frenk & White 2012; Somerville & Davé 2015; Naab & Ostriker 2017). In this framework, galaxies reside in dark matter halos, and the growth of galaxies is closely related to the growth of their host halos. Thus, the precise measurement of the galaxy–halo connection is one of the most important issues in galaxy formation (Wechsler & Tinker 2018). Moreover, accurate constraints on the the galaxy–halo connection can in turn benefit cosmology studies, such as galaxy–galaxy gravitational lensing (Bartelmann & Schneider 2001; Treu 2010) and the redshift space distortion of galaxy distributions (Kaiser 1987; Scoccimarro 2004), by connecting the observations of galaxies to theories of dark matter halos.

The stellar–halo mass relation (SHMR) is one of the most commonly used relations for populating galaxies to halos, in which larger halos host more massive galaxies, with a relatively tight scatter. Various methods have been used to model the SHMR at different redshifts, including abundance matching (AM; Guo et al. 2010; Wang & Jing 2010), the conditional luminosity function (Yang et al. 2012), and empirical modeling (EM; Behroozi et al. 2013; Moster et al. 2013, 2018; Behroozi et al. 2019). No matter how the methods are implemented, they all rely on measurements of observables, such as the galaxy stellar mass function (GSMF) and galaxy clustering (GC). Although relatively tight constraints have been achieved at the high-mass end of the SHMR for local $z_s \approx 0$, the results at the low-mass end still vary widely between studies (e.g., Guo et al. 2010; Yang et al. 2012; Moster et al. 2013; Behroozi et al. 2019) , due to the lack of accurate measurements of the GSMF and GC at the faint end. At higher redshifts, the measurement of SHMR is more difficult and more uncertain, since a large stellar mass–limited redshift sample does not exist.

Measurements of the GSMF and GC rely on accurate redshift information. Over the past two decades, there has been significant progress in spectroscopic surveys (York et al. 2000; Colless et al. 2001; Steidel et al. 2003; Le Fèvre et al. 2005; Bolton et al. 2012; Ahn et al. 2012; Garilli et al. 2014; Takada et al. 2014; DESI Collaboration et al. 2016; Ahumada et al. 2020). In the local universe ($z_s \sim 0$), the measurements of the GSMF and GC are mainly from large spectroscopic surveys, in particular the Sloan Digital Sky Survey (SDSS; York et al. 2000) and the Two Degree Field galaxy spectroscopic survey (Colless et al. 2001), down to $10^{9.0}M_\odot$ (Cole et al. 2001; Norberg et al. 2002; Li et al. 2006; Baldry et al. 2008; Li & White 2009). However, for faint galaxies, the accuracy of the measurements, especially the GC, is still very limited by survey volume. At intermediate redshifts ($z_s < 1.0$), deeper spectroscopic surveys begin to dominate the measurements. The DEEP2 galaxy spectroscopic survey (Davis et al. 2003), the VIMOS-VLT Deep Survey (Le Fèvre et al. 2005), and the

VIMOS Public Extragalactic spectroscopic survey (Garilli et al. 2014) have been used to successfully measure the GCs and GSMFs for galaxies down to $10^{10.0}M_{\odot}$ (Pozzetti et al. 2007; Meneux et al. 2008; Marulli et al. 2013; Davidzon et al. 2013; Mostek et al. 2013), though the measurements are limited by the survey volumes at the high–stellar mass end (i.e., $>10^{11.0}M_{\odot}$). Similarly, measuring the GC and GSMF at the faint end (i.e., $<10^{10.0}M_{\odot}$) is also very challenging at $z_s \sim 0.5$, for the magnitude-limited redshift surveys.

Many attempts have been made to push the measurement of the GSMF to higher redshifts ($z_s > 1.0$), by using deep multiband photometric surveys (Fontana et al. 2006; Ilbert et al. 2013; Muzzin et al. 2013; Tomczak et al. 2014; Mortlock et al. 2015; Davidzon et al. 2017; Wright et al. 2018; Leja et al. 2020; McLeod et al. 2021; Shuntov et al. 2022), which are usually deeper and more complete in terms of the stellar mass. However, the deep multiband photometric surveys usually have very small survey areas (1–2deg^2), since they require long exposure times to reach very faint sources and multiple bands, from UV to IR, to obtain relatively accurate photometric redshifts (photoz) for faint objects. Thus, the cosmic variance could be significant, especially for massive galaxies. In addition, although faint sources are detected in the deep photometric surveys, the photometric redshifts derived for them are usually trained with the spectroscopic data, which may not be complete for all types of faint sources, and therefore lead to larger photoz errors. These effects may all introduce uncertainties into the measurements of the GSMF and GC.

Systematic bias between the measurements of different surveys can also affect the study of the SHMR. Many studies (Yang et al. 2012; Behroozi et al. 2013; Moster et al. 2013, 2018; Behroozi et al. 2019) have collected GSMF measurements from different surveys at different redshifts, to model the evolution of the SHMR. However, as shown in Xu et al. (2022a; hereafter, Paper III), the systematic bias of the GSMF is still very large (∼30%) between different studies at the high-mass end, even after careful calibration, which may significantly influence the results for the SHMR.

In Xu et al. (2022b; hereafter, Paper I), on the basis of Wang et al. (2011), we developed a method named Photometric objects Around Cosmic webs (PAC), to estimate the excess surface density $\bar{n}_2 w_{\rm p}$ of photometric objects with certain physical properties around spectroscopically identified sources, which can make full use of spectroscopic and deeper photometric surveys. With PAC, we can measure $\bar{n}_2 w_{\rm p}$ for galaxies to a much lower stellar mass than when using a spectroscopic survey only. Another advantage is that $\bar{n}_2 w_{\rm p}$ is measured in a uniform way at different redshifts, since the same photometric catalog and the same analysis method (i.e. the stellar mass measurement method) are used. Obviously, the quantity contains the desired information about both the GSMF and GC.

In this paper, we will measure $\bar{n}_2 w_{\rm p}$ at different redshifts, using the Dark Energy Camera Legacy Survey (DECaLS) photometric catalogs and SDSS Main, LOWZ, and CMASS spectroscopic samples. We will then model the PAC measurements, using the abundance matching method, and constrain the evolution of the SHMR. We will compare the derived GSMF with the model-independent measurements from Paper III, to test the reliability of the results, and we will show how much we can extend the GSMF to a small stellar mass in this study. Based on our SHMR and GSMF, we will also derive the stellar mass completeness and halo occupation distributions (HODs; Jing et al. 1998; Ma & Fry 2000; Peacock & Smith 2000; Seljak 2000; Berlind & Weinberg 2002; Yang et al. 2003; Zheng et al. 2005; Zu & Mandelbaum 2015) for the LOWZ and CMASS samples, which can be useful for cosmological interpretations of their clustering and lensing measurements.

We introduce the PAC method and show the measurements in Section 2. In Section 3, we model the measurements in an N-body simulation and give the SHMR. In Section 4, we derive the HODs of the spectroscopic samples. We briefly summarize our results in Section 5. We adopt a cosmology with $\Omega_m = 0.268$, $\Omega_\Lambda = 0.732$, and $H_0 = 71\ {\rm km\ s^{-1}\ Mpc^{-1}}$ throughout the paper.

2. Observation and Measurements

In this section, we first give a brief summary of the PAC method and the spectroscopic and photometric samples used in this work. We then investigate the stellar mass completeness of the samples and present the final PAC measurements.

2.1. PAC

Supposing that we want to study two populations of galaxies, one ($\rm pop_1$) from a spectroscopic catalog and the other ($\rm pop_2$) from a photometric catalog, within a relatively narrow redshift range. We proposed a method called PAC in Paper I, which can accurately measure the excess surface density $\bar{n}_2 w_{\rm p}(r_{\rm p})$ of $\rm pop_2$ around $\rm pop_1$ with certain physical properties:

$$\bar{n}_2 w_{\rm p}(r_{\rm p}) = \frac{\bar{S}_2}{r_1^2} w_{12,\rm weight}(\theta), \tag{1}$$

where $\bar{n}_2$ and $\bar{S}_2$ are the mean number density and the mean angular surface density of $\rm pop_2$, r_1 is the comoving distance to $\rm pop_1$, and $w_{\rm p}(r_{\rm p})$ and $w_{12,\rm weight}(\theta)$ are the projected cross-correlation function and the weighted angular cross-correlation function (ACCF) between $\rm pop_1$ and $\rm pop_2$, with $r_{\rm p} = r_1\theta$. Since $\rm pop_1$ has a redshift distribution, $w_{12}(\theta)$ is weighted by $1/r_1^2$, to account for the effect that, at fixed θ, $r_{\rm p}$ varies with r_1. Using PAC, we can measure the rest-frame physical properties of $\rm pop_2$ statistically, without needing the redshift information for $\rm pop_2$, as we can make full use of deep photometric surveys. The main steps of PAC are as follows:

1. Split $\rm pop_1$ into narrower redshift bins, mainly accounting for the fast change of r_1 with redshift.
2. Assuming that all objects in $\rm pop_2$ have the same redshift as the mean redshift of each redshift bin, calculate the physical properties of $\rm pop_2$, using methods such as the spectral energy distribution (SED). In each redshift bin of $\rm pop_1$, therefore, there is a physical property catalog of $\rm pop_2$.
3. In each redshift bin, select $\rm pop_2$ with certain physical properties and calculate $\bar{n}_2 w_{\rm p}(r_{\rm p})$ according to Equation (1). The foreground and background objects with incorrect properties are canceled out through ACCF, so that only objects around $\rm pop_1$ in $\rm pop_2$ remain, which have the correct redshifts.
4. Combine the results from the different redshift bins by averaging with proper weights.

For more details, refer to Paper I.

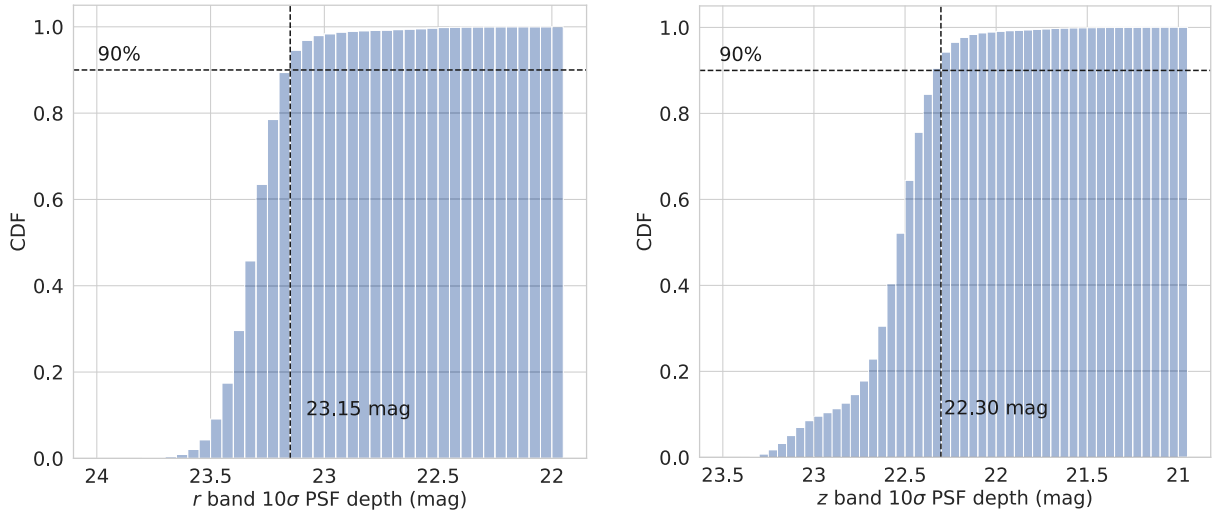

Figure 1. Cumulative distribution functions of the r-band (left) and z-band (right) 10σ point-source depths for DECaLS.

Table 1
Final Designs for the PAC Measurements

Redshift	Survey	pop_1[a] ($M_\odot$)	pop_2[b] ($M_\odot$)	PAC Redshift Bins
[0.05, 0.2]	Main	$[10^{10.3}, 10^{11.3}]$	$[10^{7.9}, 10^{11.7}]$	[0.05, 0.075], [0.075, 0.1], [0.1, 0.15], [0.15, 0.2]
[0.2, 0.4]	LOWZ	$[10^{11.3}, 10^{11.9}]$	$[10^{9.1}, 10^{11.9}]$	[0.2, 0.3], [0.3, 0.4]
[0.5, 0.7]	CMASS	$[10^{11.3}, 10^{11.9}]$	$[10^{9.7}, 10^{11.9}]$	[0.5, 0.6], [0.6, 0.7]

Notes.
[a] The stellar mass ranges of pop_1, with a fiducial equal logarithmic bin width of $10^{0.2}M_\odot$.
[b] The stellar mass ranges of pop_2, with a fiducial equal logarithmic bin width of $10^{0.2}M_\odot$.

2.2. Spectroscopic and Photometric Samples

In this work, we use the same spectroscopic and photometric data as used in Paper III. We summarize the key features in the following.

For the photometric data, we use photometric catalog[3] of DECaLS, from Data Release 9 of the DESI Legacy Imaging Survey (Dey et al. 2019). This observes around 9000 deg^2 in both the northern and southern Galactic caps (NGC and SGC, respectively), at decl. $\leqslant 32$ deg, in the g, r, and z bands, with median 5σ point-source depths of 24.9, 24.2, and 23.3 respectively. DECaLS also includes the data from the deeper Dark Energy Survey (DES; Dark Energy Survey Collaboration et al. 2016), covering an additional 5000 deg^2 in the SGC. The images are processed, using `Tractor`[4] (Lang et al. 2016) to perform source extraction. The sources are then modeled with parametric profiles convolved with a specific point-spread function (PSF), including a delta function for the point source, an exponential law, the de Vaucouleurs law, and a Sérsic profile. We use their best-fit model magnitudes throughout the paper. We only use the footprints that have been observed at least once in all three bands, and we apply a bright star mask and a bad pixel mask to the catalog using the MASKBITS[5] provided by the legacy surveys. Additional masks are used to match the geometry of the spectroscopic sample at each redshift. Galactic extinction is corrected for all sources, using the maps of Schlegel et al. (1998). To reject stars, we exclude sources with PSF morphologies, and we adopt color cuts in the $r-z$ versus $z-W1$ diagram calibrated in Paper III (see Figure 1) to further remove stellar objects, using $W1$-band data from the Wide-field Infrared Survey Explorer (Wright et al. 2010). The stars have

$$(z - W1 < 0.8 \times (r - z) - 1.0) \text{ and } (r - z > 1.0). \quad (2)$$

For spectroscopic data, all the catalogs used in this work are from SDSS (York et al. 2000). We use the SDSS Data Release 7 (DR7) Main sample[6] (Abazajian et al. 2009) and the SDSS III BOSS Data Release 12 LOWZ and CMASS samples[7] (Alam et al. 2015; Reid et al. 2016) for three redshift ranges—$z_s < 0.2$, $0.2 < z_s < 0.4$, and $0.5 < z_s < 0.7$, respectively.[8] All three samples are selected with decl. $\leqslant 32°$, to match the footprint of DECaLS, and only the NGC part is used for the Main sample, as the SGC part is very small (532 deg^2). The spectroscopic sources are crossmatched with DECaLS to obtain the g-, r-, and z-band flux measurements.

2.3. Completeness and Design

Based on the test in Figure 3 of Paper I, we split the LOWZ and CMASS samples into two and the Main sample into four narrower redshift bins, as listed in Table 1. According to the stellar mass distributions (Figure 2 of Paper III), we choose the stellar mass range of pop_1 to be $[10^{10.3}, 10^{11.3}]M_\odot$ for the Main

[3] https://www.legacysurvey.org/dr9/catalogs/
[4] https://github.com/dstndstn/tractor
[5] https://www.legacysurvey.org/dr9/bitmasks/
[6] http://sdss.physics.nyu.edu/lss/dr72/bright/
[7] https://data.sdss.org/sas/dr12/boss/lss/
[8] Throughout the paper, we use z_s for the spectroscopic redshift and z for the z-band magnitude.

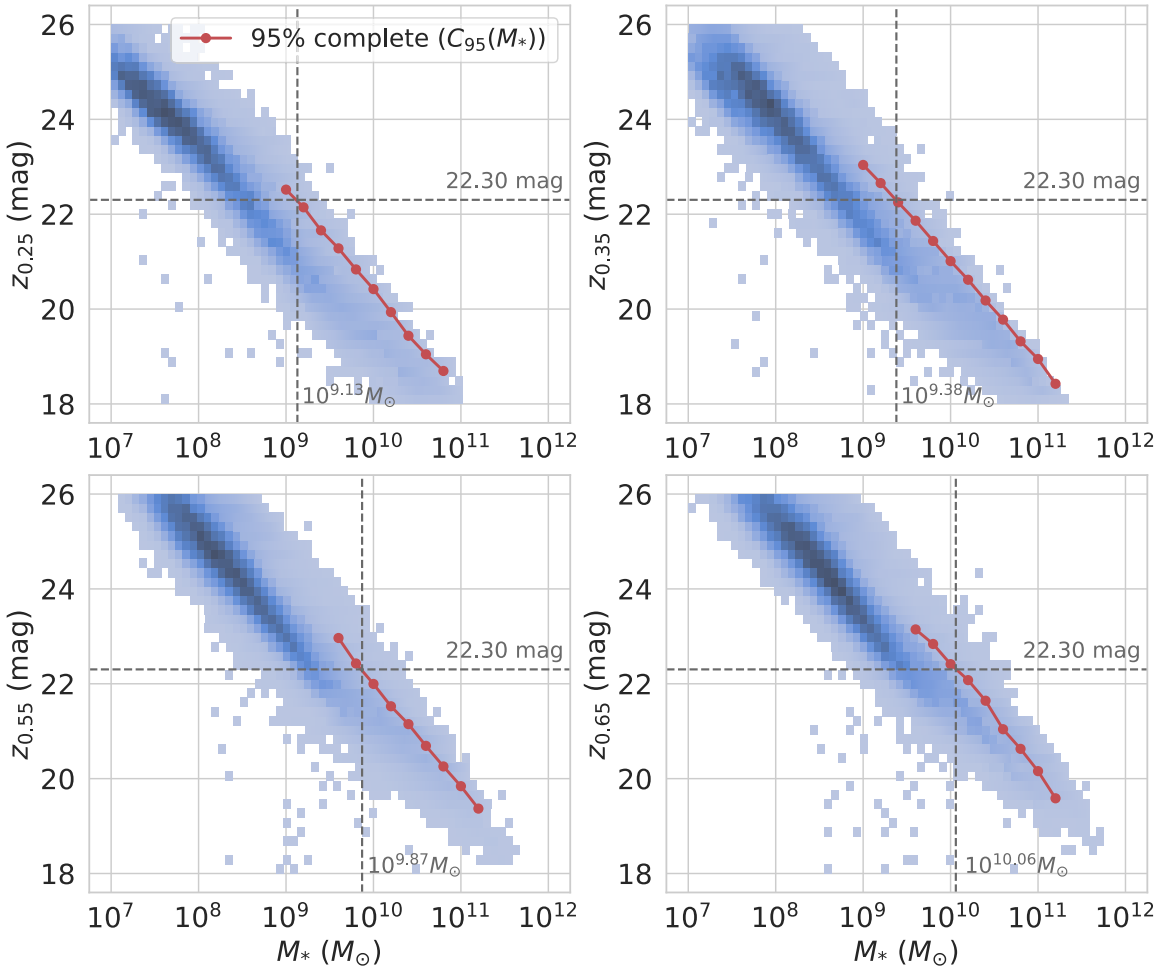

Figure 2. Stellar mass–z-band magnitude relations for the DES Deep-Fields galaxies in redshift ranges of [0.2, 0.3], [0.3, 0.4], [0.5, 0.6], and [0.6, 0.7]. The red lines with dots show the 95% completeness limits $C_{95}(M_*)$, varying with stellar mass at each redshift. The gray dashed lines show the stellar mass limits for DECaLS, with a z-band depth of 22.30 mag.

sample and $[10^{11.3}, 10^{11.9}]M_\odot$ for the LOWZ and CMASS samples, and we further split them into several stellar mass bins, with equal logarithmic intervals of 0.2.

As in Paper I and Paper III, we use the r-band (for $z_s < 0.2$) and z-band (for $0.2 < z_s < 0.4$ and $0.5 < z_s < 0.7$) 10σ point-source depths of DECaLS to study the mass completeness of pop$_2$. As shown in Figure 1, 90% of the regions in DECaLS are deeper than 23.15 mag and 22.30 mag in the r band and the z band, respectively. Thus, we use $r = 23.15$ and $z = 22.30$ as the galaxy depths for DECaLS.

In Figure 3 of Paper III, using the Galaxy And Mass Assembly Data Release 4 spectroscopic data (Driver et al. 2022), we find that for an r-band galaxy depth of 23.15 mag, the complete stellar masses are $10^{7.61}M_\odot$, $10^{7.89}M_\odot$, $10^{8.31}M_\odot$, and $10^{8.61}M_\odot$ at the redshifts 0.075, 0.1, 0.15, and 0.2. Therefore, we choose the stellar mass range of pop$_2$ to be $[10^{7.9}, 10^{11.7}]M_\odot$ for $z_s < 0.2$, where $\bar{n}_2 w_p$ is only calculated at $z_s < 0.1$ and $z_s < 0.15$ for $M_* < 10^{8.3}M_\odot$ and $M_* < 10^{8.5}M_\odot$ (See Appendix A for a validation).

The stellar mass limits that DECaLS can reach at $0.2 < z_s < 0.4$ and $0.5 < z_s < 0.7$ with a z-band depth of 22.30 mag have yet to be investigated. We use the DES Year 3 Deep-Fields catalogs[9] (Hartley et al. 2022) with photometric redshifts to explore the mass completeness in these redshift ranges. DES Deep can reach a 10σ z-band 2″ source depth of 24.3 mag, much deeper than DECaLS, and we use the regions with full eight-band *ugrizJHK$_s$* coverage (5.88 deg^2) to obtain more reliable photoz measurements. We adopt the photoz computed using EAZY (Brammer et al. 2008), provided by DES, and we calculate the physical properties using the SED code CIGALE (Boquien et al. 2019), with only the *grz* band fluxes being consistent with DECaLS. We use the Bruzual & Charlot (2003) stellar population synthesis models, with a Chabrier (2003) initial mass function and a delayed star formation history $\phi(t) \approx t \exp -t/\tau$. We adopt three metallicities, $Z/Z_\odot = 0.4$, 1, and 2.5, where $Z_\odot$ is the metallicity of the Sun. And we use the Calzetti et al. (2000) extinction law for dust reddening, with $0 < E(B-V) < 0.5$. In Figure 2, we show the stellar mass–z-band magnitude distributions for four redshift ranges: [0.2, 0.3], [0.3, 0.4], [0.5, 0.6], and [0.6, 0.7]. Following Paper I, we calculate the z-band completeness $C_{95}(M_*)$ of 95% of the galaxies being brighter than $C_{95}(M_*)$ in the z band for a given stellar mass M_* (red lines). For the DECaLS z-band galaxy depth of 22.30 mag, the complete stellar masses are $10^{9.13}M_\odot$, $10^{9.38}M_\odot$, $10^{9.87}M_\odot$, and $10^{10.06}M_\odot$ for the four redshifts. Thus, we choose the stellar mass ranges of pop$_2$ to be $[10^{9.1}, 10^{11.9}]M_\odot$ and $[10^{9.7}, 10^{11.9}]M_\odot$ for the LOWZ and CMASS redshift ranges, respectively, while only measurements at $z_s < 0.3$ and $z_s < 0.6$ are used for $M_* < 10^{9.3}M_\odot$ and $M_* < 10^{9.9}M_\odot$.

[9] https://des.ncsa.illinois.edu/releases/y3a2/Y3deepfields

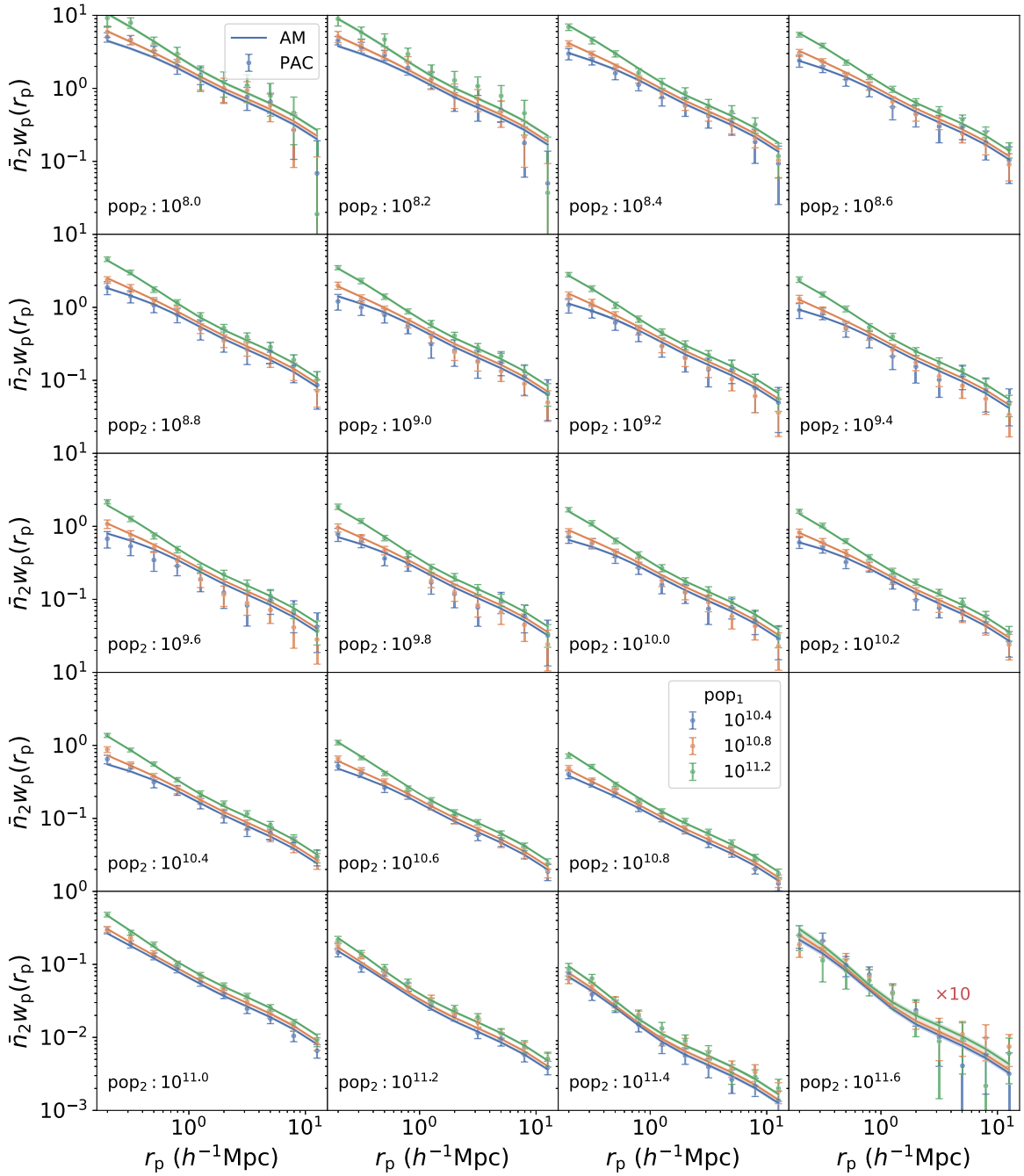

Figure 3. PAC measurements and fittings from the BP13 model for the Main sample redshift range ($z_s < 0.2$), according to the designs in Table 1. The dots with error bars show the measurements and the lines with shadows are the best-fit results and 1σ errors from the abundance matching modeling. We only show the results for three pop$_1$ mass bins ($10^{10.4}$, $10^{10.8}$, $10^{11.2} M_\odot$) from the total five, for better illustration, and the results of the last pop$_2$ bins ($10^{11.6} M_\odot$) are multiplied by 10.

We also split pop$_2$ into smaller mass bins, with equal logarithmic intervals of 0.2 in $\log M_*$ at each redshift. The final designs are summarized in Table 1.

2.4. Measurements

We adopt a method similar to the one used in Paper III to combine the results at different sky regions and redshift bins and to estimate the covariance matrices.

Let $\mathcal{A} = \bar{n}_2 w_p(r_p)$, for better representation. Assuming that $\mathcal{A}$ is measured for N_r redshift bins and N_s sky regions (e.g., DECaLS NGC and DECaLS SGC), we further split each region into $N_{\rm sub}$ subregions for error estimation, using jackknife resampling. According to Equation (1), $\mathcal{A}_{i,j,k}$ can be calculated in the ith redshift bin, the jth sky region, and the kth jackknife subsample, using the Landy–Szalay estimator (Landy & Szalay 1993). We first combine the measurements at different sky regions using the region area w_s as the weight:

$$\mathcal{A}_{i,k} = \frac{\sum_{j=1}^{N_s} \mathcal{A}_{i,j,k} w_{s,j}}{\sum_{j=1}^{N_s} w_{s,j}}. \quad (3)$$

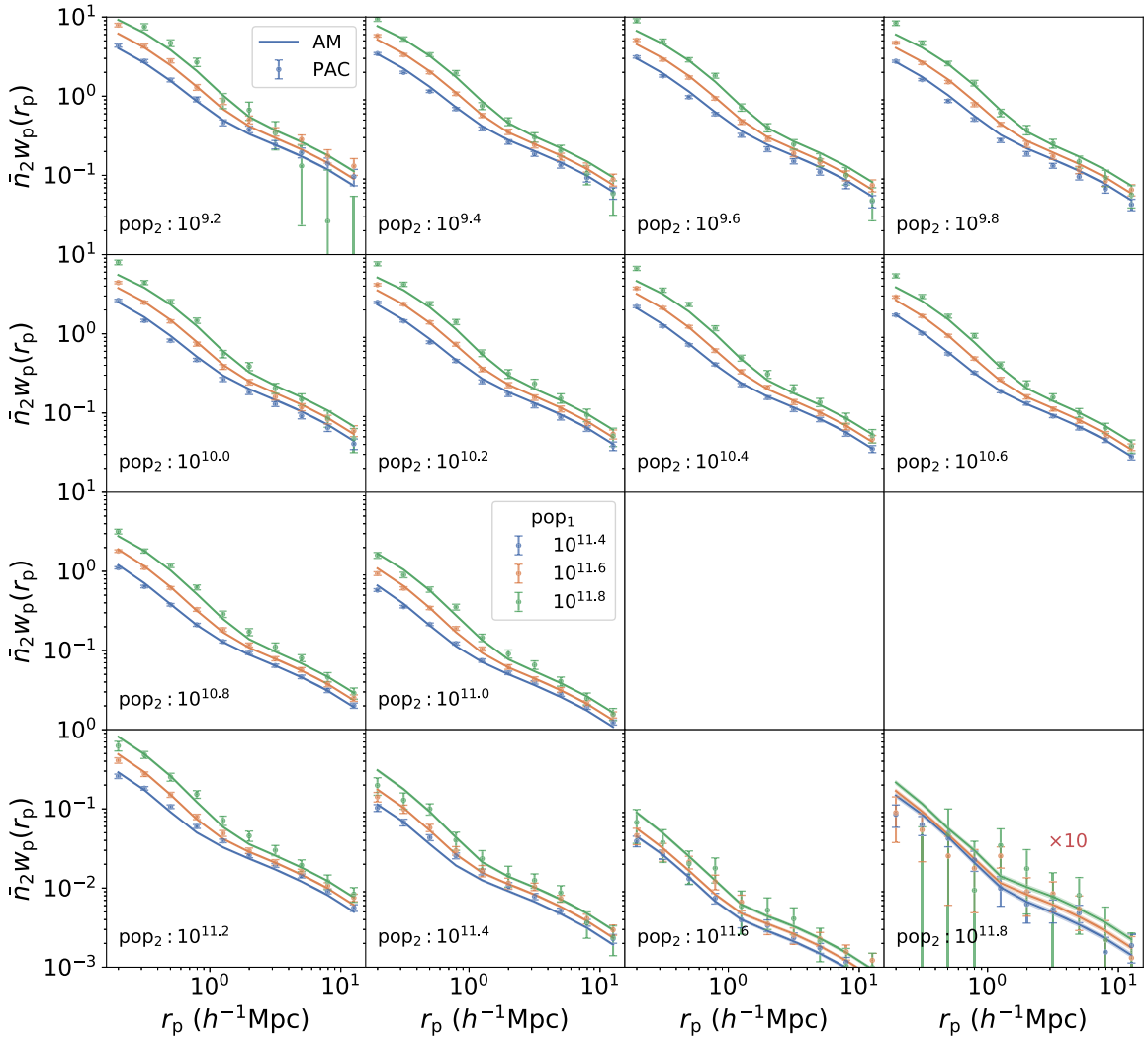

Figure 4. The same as Figure 3, but for the LOWZ redshift range ($0.2 < z_s < 0.4$).

We then estimate the mean values and the covariance matrices of the mean values for each redshift bin from $N_{\rm sub}$ subsamples:

$$\mathcal{A}_i = \sum_{k=1}^{N_{\rm sub}} \mathcal{A}_{i,k}/N_{\rm sub}, \tag{4}$$

$$C_{ab,i} = \frac{N_{\rm sub}-1}{N_{\rm sub}} \sum_{k=1}^{N_{\rm sub}} (\mathcal{A}_{i,k}(r_{\rm p}^a) - \mathcal{A}_i(r_{\rm p}^a)) \times (\mathcal{A}_{i,k}(r_{\rm p}^b) - \mathcal{A}_i(r_{\rm p}^b)), \tag{5}$$

where a and b denote the ath and bth radial bins. Finally, the results from the different redshift bins are combined according to the covariance matrices. Let $w_i(r_{\rm p}) = \sigma_i^{-1}(r_{\rm p})$, where $\sigma_i^2(r_{\rm p})$ is the diagonal component of $\boldsymbol{C}_i$,

$$\mathcal{A} = \frac{\sum_{i=1}^{N_{\rm r}} \mathcal{A}_i w_i^2}{\sum_{i=1}^{N_{\rm r}} w_i^2}, \tag{6}$$

$$C_{ab} = \frac{\sum_{i=1}^{N_{\rm r}} w_i^2(r_{\rm p}^a) w_i^2(r_{\rm p}^b) C_{ab,i}}{\sum_{i=1}^{N_{\rm r}} w_i^2(r_{\rm p}^a) \sum_{i=1}^{N_{\rm r}} w_i^2(r_{\rm p}^b)}. \tag{7}$$

According to the designs in Table 1, we measure $\bar{n}_2 w_{\rm p}(r_{\rm p})$ in the radial range of $0.1\,h^{-1}\,{\rm Mpc} < r_{\rm p} < 1\,h^{-1}\,{\rm Mpc}$, with $N_{\rm sub} = 100$ for the three redshift ranges. The measurements are extended to scales far beyond the virial radii of the halos hosting pop$_1$ galaxies, and thus include information about both centrals and satellites. The results are shown as dots with error bars in Figures 3, 4, and 5, for the Main sample, LOWZ, and CMASS, respectively. The square roots of the diagonal components of the covariance matrices are shown as the error bars. The measurements are overall good for all mass bins within the whole radial ranges.

3. Simulation and Modeling

In this section, we introduce the simulation and abundance matching method used in this work, and show the constraints on the SHMR from our PAC measurements.

3.1. CosmicGrowth Simulation

We use the `CosmicGrowth` simulation (Jing 2019) in this work to model the PAC measurements. The `CosmicGrowth` simulation suite is a grid of high-resolution N-body simulations that are run in different cosmologies, using an adaptive parallel P^{3}M code (Jing & Suto 2002). We use one of the ΛCDM simulations, with the cosmological parameters $\Omega_m = 0.268$, $\Omega_\Lambda = 0.732$, and $\sigma_8 = 0.831$ (Hinshaw et al. 2013). The box size is $600\,h^{-1}\,{\rm Mpc}$, with 3072^3 dark matter particles and a

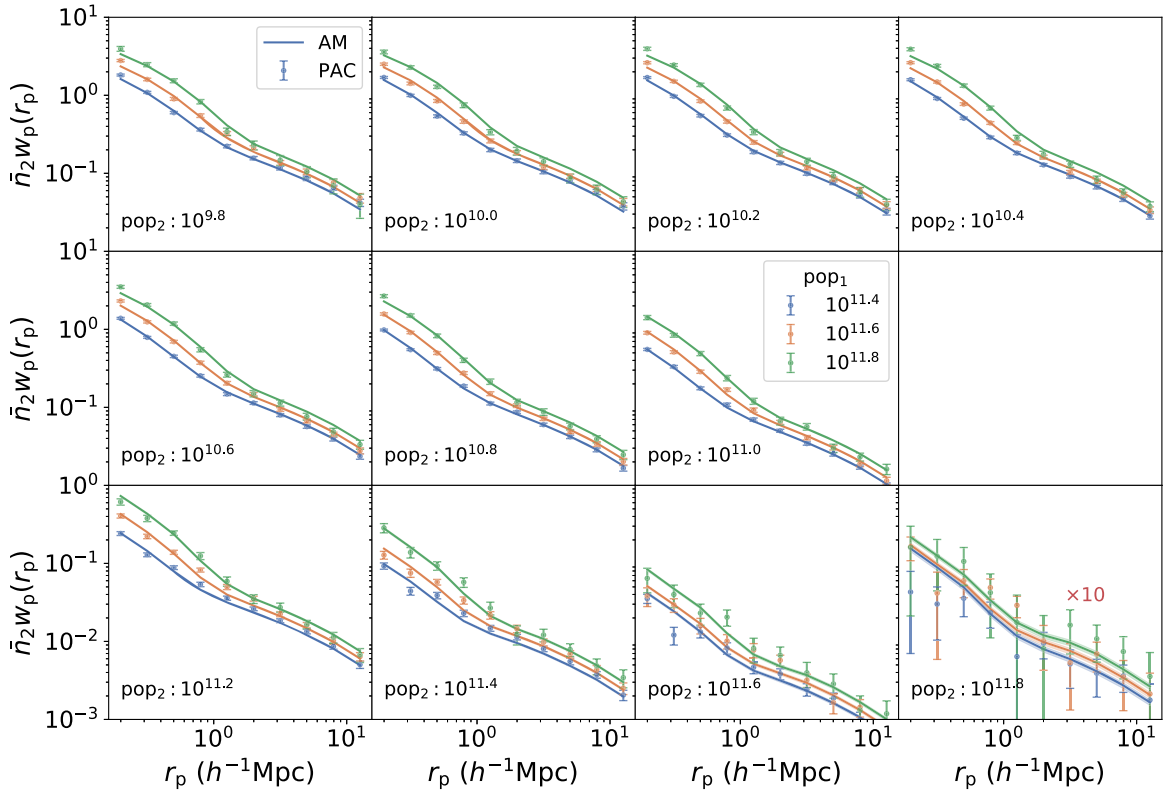

Figure 5. The same as Figure 3, but for the CMASS redshift range ($0.5 < z_s < 0.7$).

Table 2
Posterior PDFs of the Parameters from MCMC for the SHMR Models

Redshift	Model	$\log_{10}(M_0)$ ($\log_{10}(h^{-1}\,M_\odot)$)	α	δ	β	$\log_{10}(k)/\log_{10}(\epsilon)$ ($\log_{10}(M_\odot)$)/($\log_{10}(h)$)	σ
$z_s < 0.2$	BP13	$11.338^{+0.027}_{-0.028}$	$0.484^{+0.027}_{-0.025}$	$3.041^{+0.134}_{-0.128}$	$1.632^{+0.039}_{-0.041}$	$-1.545^{+0.017}_{-0.017}$	$0.237^{+0.008}_{-0.008}$
$0.2 < z_s < 0.4$	BP13	$11.359^{+0.024}_{-0.025}$	$0.623^{+0.032}_{-0.030}$	$3.248^{+0.131}_{-0.125}$	$1.702^{+0.050}_{-0.054}$	$-1.598^{+0.019}_{-0.020}$	$0.190^{+0.003}_{-0.004}$
$0.5 < z_s < 0.7$	BP13	$11.509^{+0.028}_{-0.029}$	$0.740^{+0.058}_{-0.056}$	$2.964^{+0.159}_{-0.141}$	$2.094^{+0.039}_{-0.039}$	$-1.565^{+0.022}_{-0.025}$	$0.190^{+0.004}_{-0.004}$
$z_s < 0.2$	DP	$11.732^{+0.020}_{-0.020}$	$0.299^{+0.011}_{-0.012}$		$1.917^{+0.019}_{-0.020}$	$10.303^{+0.019}_{-0.019}$	$0.233^{+0.008}_{-0.008}$
$0.2 < z_s < 0.4$	DP	$11.579^{+0.012}_{-0.012}$	$0.429^{+0.006}_{-0.006}$		$2.215^{+0.022}_{-0.022}$	$10.105^{+0.011}_{-0.010}$	$0.201^{+0.003}_{-0.004}$
$0.5 < z_s < 0.7$	DP	$11.624^{+0.010}_{-0.010}$	$0.466^{+0.008}_{-0.008}$		$2.513^{+0.034}_{-0.033}$	$10.133^{+0.010}_{-0.010}$	$0.192^{+0.004}_{-0.004}$

softening length $\eta = 0.01\,h^{-1}$ Mpc. Groups are identified using the friends-of-friends algorithm, with a linking length of 0.2 times the mean particle separation. The halos are then processed with HBT+ (Han et al. 2012, 2018), to find the subhalos and trace their evolution histories. We use the catalogs of snapshots at redshifts of about 0.12, 0.28, and 0.57 to compare with the Main sample, LOWZ, and CMASS measurements. The merger timescales of the subhalos with fewer than 20 particles, which may be unresolved, are evaluated using the fitting formula in Jiang et al. (2008), and those that have already merged into central subhalos are abandoned. The halo mass function (Figure 1 of Jing 2019) and the subhalo mass function (Figure 5 of Paper I) of the `CosmicGrowth` simulation can be robust down to at least 20 particles ($\sim 10^{10.0} h^{-1}\,M_\odot$), which is good enough for this work.

3.2. Subhalo Abundance Matching

To parameterize the SHMR, the most commonly used five-parameter formula is a double power law (DP) with a scatter (Wang & Jing 2010; Yang et al. 2012; Moster et al. 2013):

$$M_* = \left[\frac{2k}{(M_{\rm acc}/M_0)^{-\alpha} + (M_{\rm acc}/M_0)^{-\beta}}\right]. \quad (8)$$

Here, we define $M_{\rm acc}$ as the viral mass $M_{\rm vir}$ of the halo at the time when the galaxy was last the central dominant object. We use the fitting formula in Bryan & Norman (1998) to find $M_{\rm vir}$. The scatter in $\log(M_*)$ at a given $M_{\rm acc}$ is described with a Gaussian function of width σ. We also let $\alpha < \beta$, so that α and β represent the slopes of the high- and low-mass ends of the SHMR, respectively.

However, Behroozi et al. (2013; hereafter, BP13) found that the SHMR of the DP form failed to reproduce the upturn

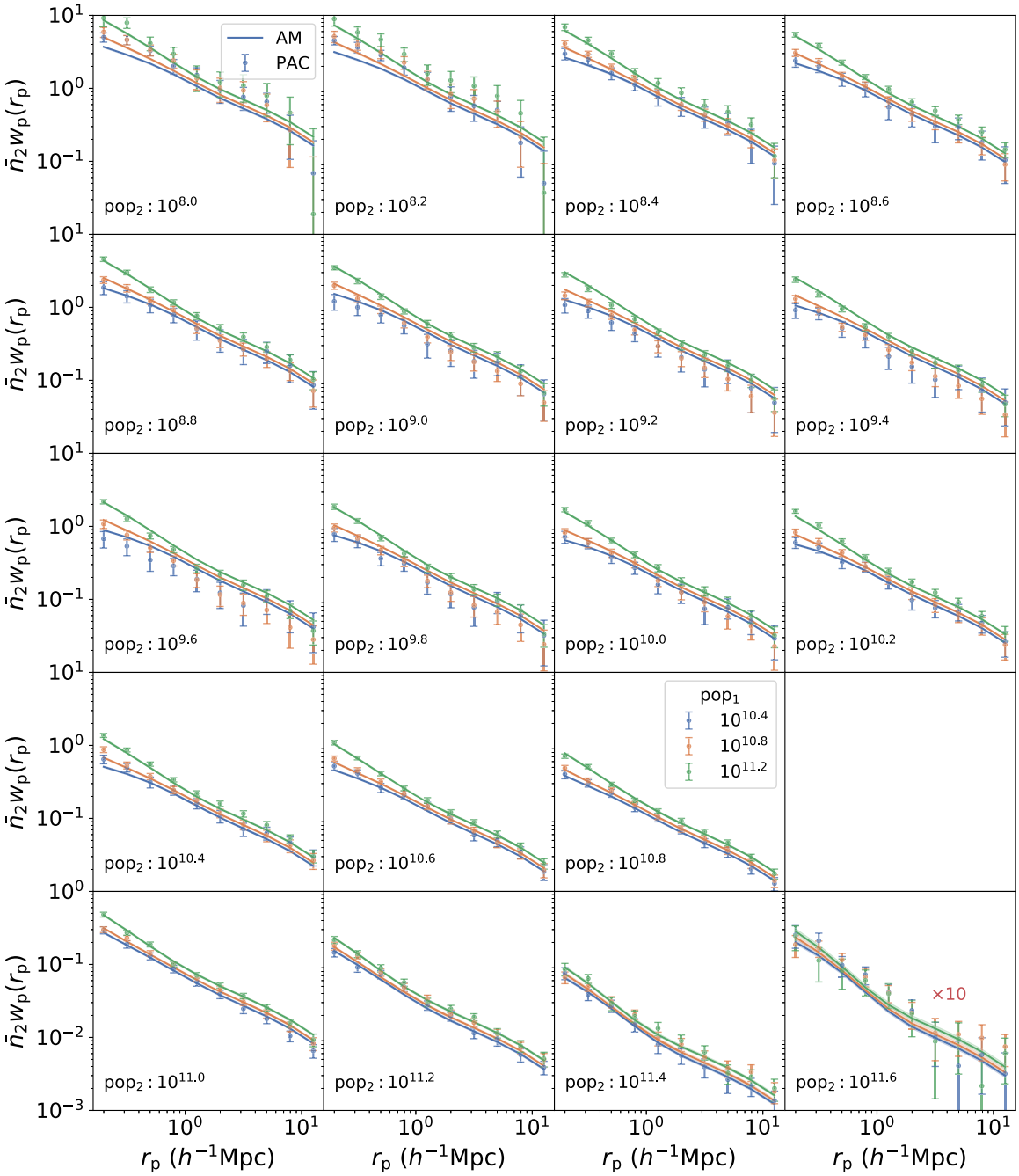

Figure 6. The same as Figure 3, but for the Main sample redshift range ($z_s < 0.2$), with fittings from the DP model.

feature in the GSMF at $M_* < 10^{9.5} M_\odot$. They provided a six-parameter formula for the SHMR of low-mass galaxies:

$$\log_{10}(M_*) = \log_{10}(\epsilon M_0) + f\left(\log_{10}\left(\frac{M_{\rm acc}}{M_0}\right)\right) - f(0)$$
$$f(x) = -\log_{10}(10^{-\beta x} + 1) + \delta \frac{(\log_{10}(1 + \exp(x)))^\alpha}{1 + \exp(10^{-x})}, \quad (9)$$

also with a scatter σ in $\log(M_*)$. At $M_{\rm acc} \ll M_0$ and $M_{\rm acc} \gg M_0$, this formula degenerates into power laws with the indices β and α.

We model the PAC measurements using both the BP13 and DP forms for the three redshift ranges. As we will show, both the BP13 and DP models are able to fit the measurements from LOWZ and CMASS equally well, while the BP13 model is strongly favored in fitting the measurements for $M_* < 10^{10} M_\odot$ in the Main sample.

In the simulation, the correlation functions are calculated using the tabulated method (Zheng & Guo 2016; Gao et al. 2022), to avoid redundant computation during the fitting process. We define χ^2 as

$$\chi^2 = \sum_{i=1}^{N_{\rm m_1}} \sum_{j=1}^{N_{\rm m_2}} (\mathcal{A}_{i,j}^{\rm PAC} - \mathcal{A}_{i,j}^{\rm AM})^T \boldsymbol{C}_{i,j}^{-1} (\mathcal{A}_{i,j}^{\rm PAC} - \mathcal{A}_{i,j}^{\rm AM}), \quad (10)$$

where N_{m_1} and N_{m_2} are the numbers of mass bins of pop$_1$ and pop$_2$, $\mathcal{A}^{\rm PAC}$ and $\mathcal{A}^{\rm AM}$ are the measurements and model predictions, $\boldsymbol{C}^{-1}$ is the inverse of the covariance matrix $\boldsymbol{C}$,

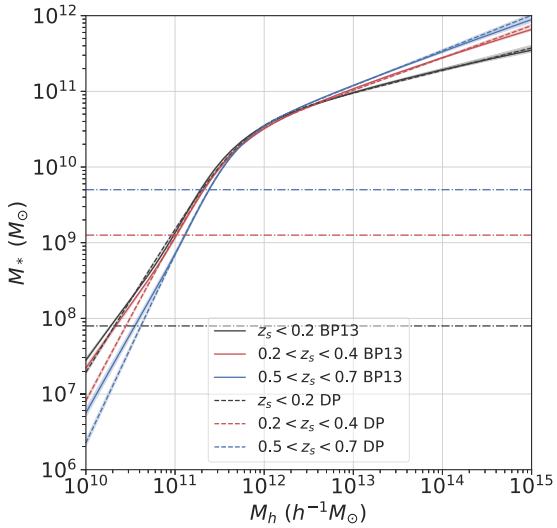

Figure 7. The mean SHMRs (lines) and 1σ errors (shadows) at different redshift ranges, from both the BP13 (solid lines) and DP (dashed lines) models. The horizontal lines indicate the stellar mass limits covered by the observation data at each redshift, matched by color.

and T denotes matrix transposition. We use the Markov Chain Monte Carlo (MCMC) sampler `emcee` (Foreman-Mackey et al. 2013) to perform maximum likelihood analyses of $\{M_0, \alpha, \beta, k, \sigma\}$ for the DP model and of $\{M_0, \alpha, \delta, \beta, \epsilon, \sigma\}$ for the BP13 model.

3.3. Evolution of the SHMR

The marginalized posterior PDFs of the parameters are listed in Table 2 for the three redshift ranges and the BP13 and DP models, and we also show the joint posterior distributions of the parameters in Appendix B, using `corner` (Foreman-Mackey 2016). The corresponding $\bar{n}_2 w_p(r_p)$ from the BP13 model in the three redshift ranges are shown as the lines with shadows in Figures 3, 4, and 5. The fitting is good overall for all the mass bins in our samples, and all the parameters are constrained well, with percent- or even subpercent-level errors. We also show the DP model fittings for the Main sample redshift range in Figure 6. We find that the DP model overpredicts the number of galaxies at $M_* = 10^{9.5} M_\odot$, while it underpredicts those at $M_* < 10^{8.6} M_\odot$. The BP13 model describes the SHMR for small galaxies better than the DP model.

The best-fit SHMRs and the 1σ errors are shown in Figure 7. The results from the BP13 and DP models are shown with the solid and dashed lines for $z_s < 0.2$ (black), $0.2 < z_s < 0.4$ (red), and $0.5 < z_s < 0.7$ (blue), respectively. We also plot the stellar mass limit covered by the observation data at each redshift with horizontal lines. In the mass ranges covered by the observation data, all the SHMRs are constrained to percent level, and the results from the BP13 and DP models are in good agreement with each other in the LOWZ and CMASS redshift ranges. However, as mentioned above, the DP model is unable to recover the upturn at the low-mass end of the SHMR in the Main sample redshift range.

Our accurate SHMR determination shows that halos with a fixed mass at the massive end ($M_h > M_0$) host more massive galaxies at higher redshifts, which quantifies the downsizing of massive galaxies. On the other hand, our result indicates an opposite trend in the evolution of small halos ($M_h < M_0$), which means that small galaxies are continuously forming from $z_s = 0.7$, although this conclusion must be treated with caution, as the mass range covered by the observation data is limited for $M_h < M_0$ at $z_s = 0.6$.

We also show the GSMFs in different redshift ranges derived from the BP13 model in Figure 8. The GSMFs from our model are all constrained to subpercent levels. The model-independent measurements from Paper III are also plotted for comparison. We find that the two measurements are in good agreement with one another at all three redshift ranges, proving that both measurements are robust over the whole mass range. At the massive end ($M_* > 10^{11.0} M_\odot$), the results from Paper III were compared with the photoz results from the DESI Legacy Imaging Survey (Zhou et al. 2021), and we found great consistency (see Figure 4 in Paper III). Thus, the three independent measurements confirm that our measurements of the GSMF at the massive end are reliable. Our measurements indicate that the GSMF has nearly no evolution from $z_s = 0.7$ for $M_* > 10^{10.6} M_\odot$ and slightly increases with decreasing redshift for smaller stellar masses. We also list the GSMFs from the BP13 model in Table C1. We also plot the GSMF at $z_s < 0.2$ from the DP model in Figure 8: it is clear that the DP model fails to capture the upturn in the GSMF, with the deviation starting from $10^{10.0} M_\odot$.

Combining the SHMR and GSMF measurements, our results favor the physical picture of massive galaxies being quenched from at least $z_s = 0.7$, while their host halos are still assembling their mass, and of low-mass galaxies still forming stars in an efficient way. Our results are inconsistent with a few previous works (BP13; Moster et al. 2013; Behroozi et al. 2019) for massive galaxies and halos. In these works, the stellar mass increases with decreasing redshift for a fixed halo mass at $M_h > M_0$. This may be due to the GSMFs that they used to constrain the SHMR at different redshifts not being well calibrated. Their GSMFs are still increasing with decreasing redshift at the massive ends. Their GSMFs are also usually from different surveys, which may have systematic bias between each other. Due to the exponentially decreasing feature of the GSMF at the massive end, a very small offset can cause a significant change in the GSMF. As we mentioned in Paper III (Appendix A), at the high-mass end, the GSMFs of the north and south parts of the DESI Legacy Imaging Surveys can still have a 30% offset, with a 500 $\deg^2$ footprint already being overlapped for calibration. Different methods for source extraction, photometry, and determining SEDs can also introduce further bias. Moreover, the GSMFs that are used at high redshifts are usually from deep spectroscopic or photometric surveys with relatively small survey areas, thus the cosmic variance may become important for the massive end. One of the advantages of measuring the SHMR using PAC is that we can provide measurements in a uniform way, so we can minimize the systematic bias between different redshifts.

In Figure 9, we compare our measurements of the SHMR to previous studies at $z_s \sim 0.1$. In these works, BP13 and Moster et al. (2013) collected the GSMF and/or cosmic star formation rate measurements from different surveys and modeled the evolution of the SHMR using EM; Guo et al. (2010) modeled the SHMR in the local universe with the SDSS DR7 GSMF (Li & White 2009) and galaxy correlations, using abundance matching; and Yang et al. (2012) constrained the evolution of the SHMR based on the GSMF and conditional stellar mass function (CSMF; Yang et al. 2009) measurements at different

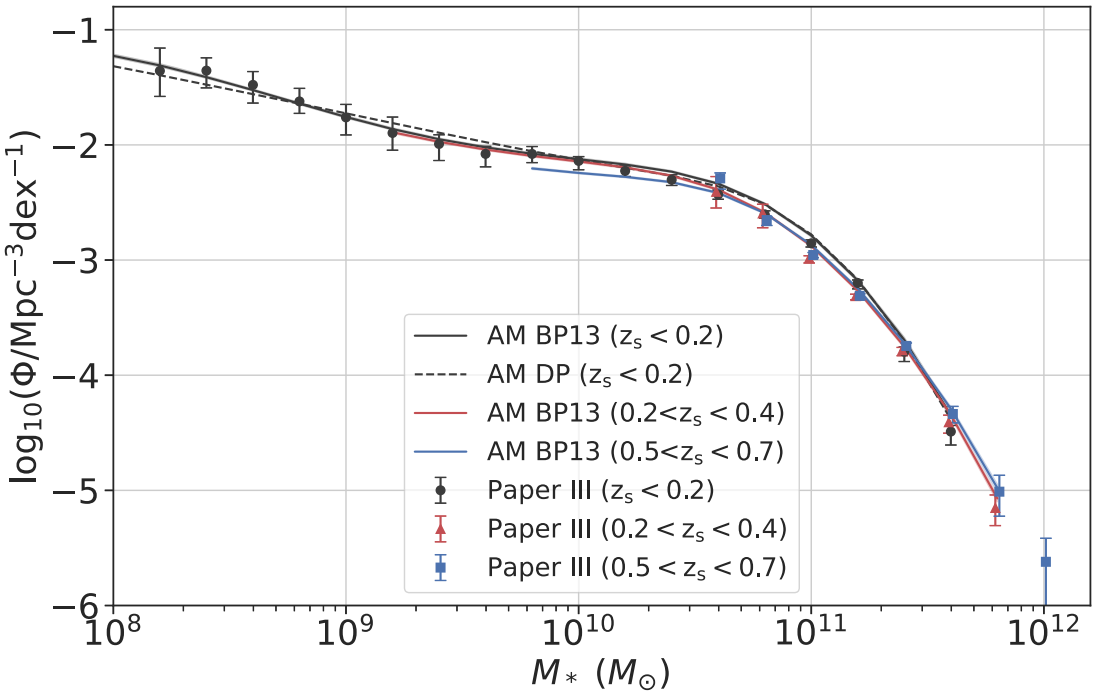

Figure 8. GSMFs (solid lines) and 1σ errors (shadows) at different redshift ranges from the BP13 model. The results from the DP model at $z_s < 0.2$ are also shown in dashed line. The model-independent measurements of GSMF from Paper III are shown for comparison as dots with error bars.

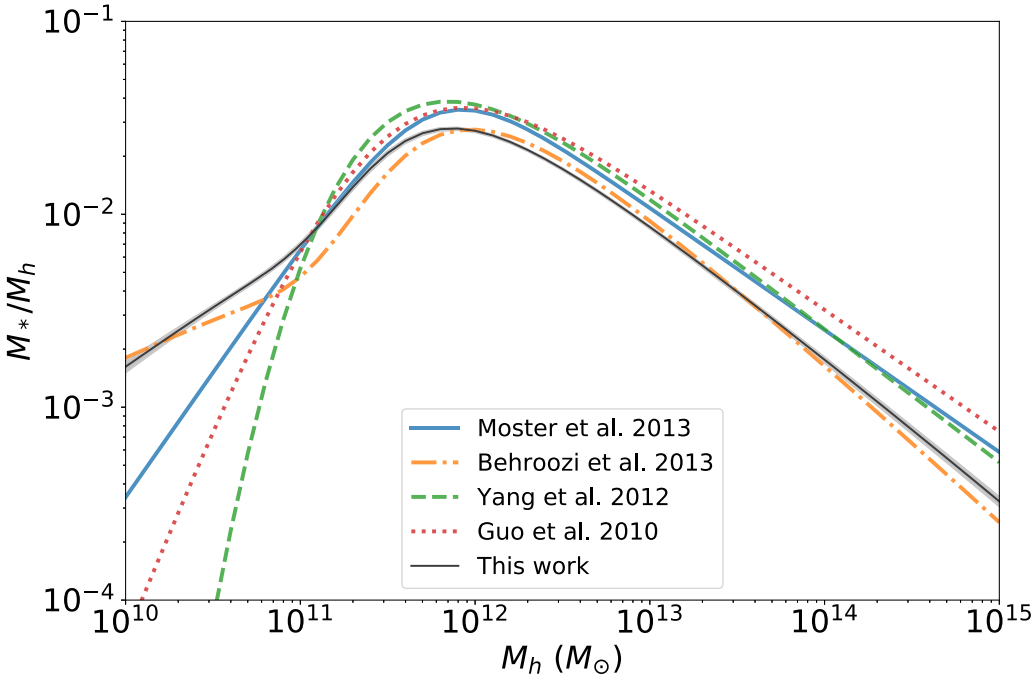

Figure 9. Comparison of our mean SHMR to previous studies at $z_s \sim 0.1$. The results compared include those from EM (BP13; Moster et al. 2013), from abundance matching (Guo et al. 2010), and from CSMF modeling (Yang et al. 2012).

redshifts. The halo masses are all corrected to $M_{\rm vir}$. However, there are still some differences in the definition of the subhalo mass. For satellites, BP13 and Moster et al. (2013) use the peak progenitor mass ($M_{\rm peak}$), while others use the last accretion mass ($M_{\rm acc}$). Here, we assume that the definition of the subhalo mass has a negligible effect.

At the high-mass end, the results from different studies are relatively consistent, since the measurements are robust for this mass range with large-area spectroscopic surveys, although discrepancies still exist that may be due to some systematics in the measurements of the stellar mass. At the low-mass end, the discrepancies between the studies are large, since the

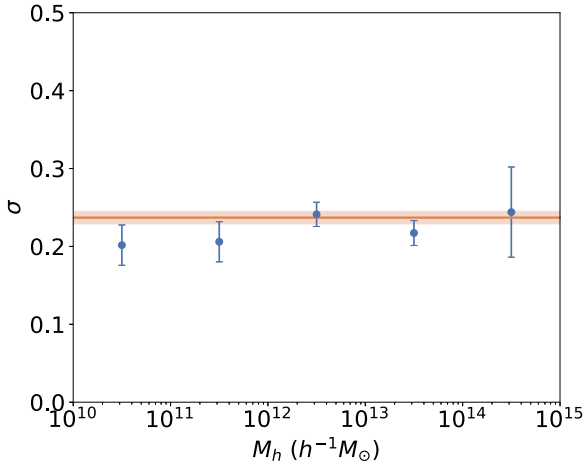

Figure 10. The halo mass dependence of the scatter in the SHMR at $z_s < 0.2$. The blue dots with error bars show the results from the multi-σ fittings. The orange line with the shadow is the previous constraint, with a single σ.

constraints are mainly from the GSMF measurements in SDSS, which are very limited ($z_s < 0.03$) for low-mass galaxies ($M_* < 10^{9.0} M_\odot$). Instead, making full use of the deep photometric data, we can give a precise measurement of the SHMR at the low-mass end with PAC.

3.4. Halo Mass Dependence of the Scatter

The SHMR models that we use above adopt a constant scatter σ. However, whether the scatter depends on the halo mass or not is still under debate. Thus, we model the PAC measurements at $z_s < 0.2$, again with the BP13 model, but with five different scatters for the halo mass ranges of $[10^{10.0}, 10^{11.0}]h^{-1}\,M_\odot$, $[10^{11.0}, 10^{12.0}]h^{-1}\,M_\odot$, $[10^{12.0}, 10^{13.0}]h^{-1}\,M_\odot$, $[10^{13.0}, 10^{14.0}]h^{-1}\,M_\odot$, and $[10^{14.0}, 10^{15.0}]h^{-1}\,M_\odot$, respectively. The results are shown in Figure 10. With the very accurate measurements, we find nearly no dependence of the scatter on the halo mass down to $10^{10.0}h^{-1}\,M_\odot$. The scatters are all within 0.2–0.25, and they are consistent with the results from the previous single-scatter model.

4. HODs of the LOWZ and CMASS Samples

The HODs of the LOWZ and CMASS samples are still under debate (Leauthaud et al. 2016; Guo et al. 2018), due to the stellar mass incompleteness, and the reliability of the HODs can influence cosmology studies, in terms of the galaxy–galaxy lensing and the redshift space distortion. With the GSMFs measured in Paper III and the SHMRs measured in this work, we can derive the stellar mass incompleteness and the HODs for the LOWZ and CMASS samples.

4.1. Stellar Mass Completeness

We first calculate the stellar mass completeness for the LOWZ and CMASS samples. We adopt the GSMFs measured in Paper III as complete references. For $M_* = 10^{12} M_\odot$, as discussed in Paper III (Figure 4), the photoz measurement for the GSMFs is more reliable, and adopted here, because the number of massive galaxies is very limited in the survey for the two-point statistics.

We present the GSMFs of the LOWZ and CMASS samples in different redshift ranges in the top panels of Figure 11, along with our GSMFs from Paper III. We then derive the stellar mass completeness in the bottom panels, and also list them in Table D1. The errors are all estimated using jackknife resampling. The completeness in general increases with stellar mass and is peaked at around $10^{11.6} M_\odot$. The peak completeness is around 85% for LOWZ and around 80% for CMASS. Neither the LOWZ nor the CMASS samples are complete even at the highest stellar mass $M_* = 10^{11.8} M_\odot$ and $10^{12.0} M_\odot$, and the incompleteness is even worse at $10^{12.0} M_\odot$, especially at the lower-redshift bins ($z_s = 0.25$ for LOWZ and $z_s = 0.55$ for CMASS). In Table D2, we mimic the target selection process for the CMASS sample of $10^{11.8} M_\odot$ and $10^{12.0} M_\odot$, using the DECaLS photoz sample. We find that the target selection for spectroscopic observations removes 11.5% and 11.2% of the galaxies, and that only 89.7% and 81.3% of the selected sources have successful redshift measurements, respectively. The two effects combined result in about 79% and 76% completeness, respectively, which is consistent with our measurement in Figure 11. Therefore, at least for CMASS, the lower completeness at $10^{12.0} M_\odot$ may be due to less spectral identification.

We also compare our stellar mass completeness with previous works (Leauthaud et al. 2016; Guo et al. 2018) in Figure 12. Qualitatively, the three studies yield similar incompleteness trends. Quantitatively, the results for LOWZ from the different studies are consistent with each other, while the differences are larger for CMASS. The reason for the differences is not clear. Their results might be sensitive to the total GSMFs used in Leauthaud et al. (2016) and the formula used to model the completeness in Guo et al. (2018).

4.2. HODs

In combination with the stellar mass completeness, we can derive the HODs for the LOWZ and CMASS samples from our SHMRs. We use the completeness for the redshift ranges of $0.2 < z_s < 0.4$ and $0.5 < z_s < 0.7$ for the LOWZ and CMASS samples, respectively, and assume that the galaxies are randomly selected. The HODs for the LOWZ and CMASS samples are shown in Figure 13.

As an example, we also compare with a recent HOD for CMASS galaxies (the dotted lines in Figure 13), presented by Yuan et al. (2022a), who adopted the standard form of Zheng et al. (2007). Yuan et al. (2022a) constrained the cosmological parameters and the HOD parameters simultaneously, using the emulator based on the `ABACUSHOD` framework (Yuan et al. 2022b) in the `ABACUSSUMMIT` simulation suite (Maksimova et al. 2021). We find that both the amplitude and the shape of our HOD are different from those of Yuan et al. (2022a). The difference may have mainly been caused by the fact that they did not consider the stellar mass incompleteness. It would be interesting to investigate how much the incompleteness impacts the determination of cosmological parameters. Cosmological probes, such as galaxy–galaxy lensing and redshift space distortion, are especially sensitive to the HOD or the stellar mass completeness. With the accurately measured SHMR and stellar mass completeness, we will revisit this question in a future work.

5. Summary

In this work, using the SDSS Main, LOWZ, and CMASS spectroscopic samples, with DECaLS photometric data, we measure $\bar{n}_2 w_p$ down to the stellar masses $10^{8.0} M_\odot$, $10^{9.2} M_\odot$,

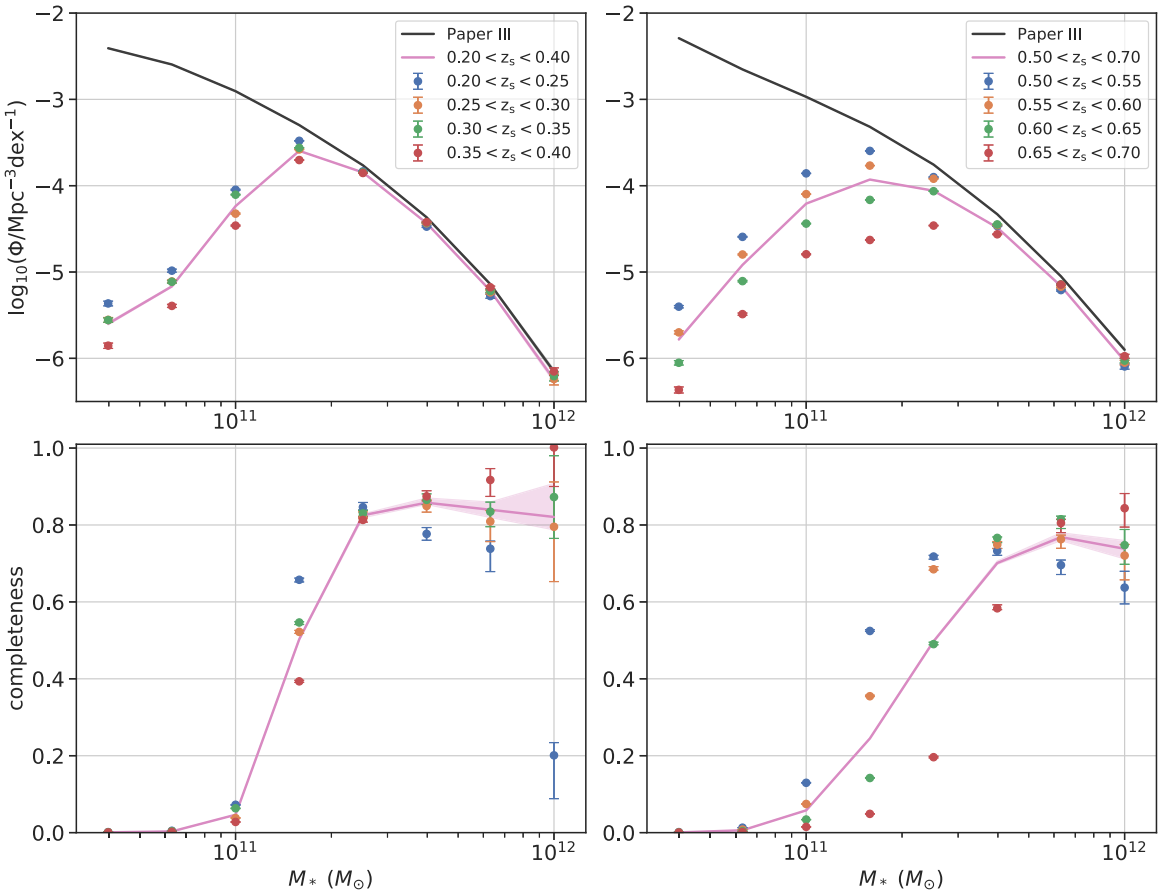

Figure 11. Top: GSMFs of the LOWZ (left) and CMASS (right) samples in different redshift ranges, compared to the DECaLS photoz measurements in Paper III ($0.2 < z_p < 0.4$ and $0.5 < z_p < 0.7$). Bottom: stellar mass completeness of the LOWZ (left) and CMASS (right) samples.

and $10^{9.8} M_\odot$ for the redshift ranges $z_s < 0.2$, $0.2 < z_s < 0.4$, and $0.5 < z_s < 0.7$, respectively. We model the $\bar{n}_2 w_p$ with the abundance matching method in an N-body simulation, and we accurately constrain the evolution of the SHMR. We summarize our results as follows.

1. The parameters of the SHMRs are well constrained (at the percent level) for all the redshift ranges. According to our results, halos with fixed halo masses host more massive galaxies at higher redshifts for the high-mass end ($M_h > M_0$), with the trend being reversed at the low-mass end ($M_h < M_0$). This quantifies the downsizing of massive galaxies from $z_s = 0.7$, and indicates that small galaxies are still growing faster than their host halos.
2. With our precise measurement of $\bar{n}_2 w_p$ down to a stellar mass of $10^{8.0} M_\odot$ in the local universe ($z_s < 0.2$), we find that the form of BP13 describes the SHMR at low mass much better than the DP form.
3. Adopting a halo mass–dependent scatter of the SHMR, we demonstrate that the scatter does not vary with halo mass in the wide mass range of $[10^{10.0}, 10^{15.0}]h^{-1} M_\odot$ at high precision, which supports the constant scatter that has been assumed in many previous studies being a good approximation.
4. The derived GSMFs from our SHMRs are in perfect agreement with the model-independent measurements in Paper III at all three redshifts, but the present study extends the GSMF measurements to lower stellar mass. Our results show that the GSMF has little evolution at the massive end $M_* > 10^{10.5} M_\odot$ from $z_s = 0.7$.
5. With accurate SHMR and GSMF measurements, we calculate the stellar mass completeness and HODs for the LOWZ and CMASS samples. We find that the standard HOD modeling may lead to a biased result, without properly taking into account the stellar mass completeness. Our SHMR and stellar mass completeness measurements will be useful in correctly interpreting cosmological measurements, such as by modeling galaxy–galaxy lensing and redshift space distortion, based on these samples.

With the next generation of larger and deeper spectroscopic and photometric surveys, such as the Dark Energy Spectroscopic Instrument (DESI Collaboration et al. 2016), the Legacy Survey of Space and Time (Ivezić et al. 2019), and Euclid (Laureijs et al. 2011), we will be able to use the PAC method to explore the galaxy–halo connection at higher redshifts and lower masses.

The work is supported by the NSFC (grant Nos. 12133006, 11890691, and 11621303) and by 111 project No. B20019. We gratefully acknowledge the support of the Key Laboratory for Particle Physics, Astrophysics and Cosmology, Ministry of Education. This work has made use of the Gravity Supercomputer at the Department of Astronomy, Shanghai Jiao Tong University.

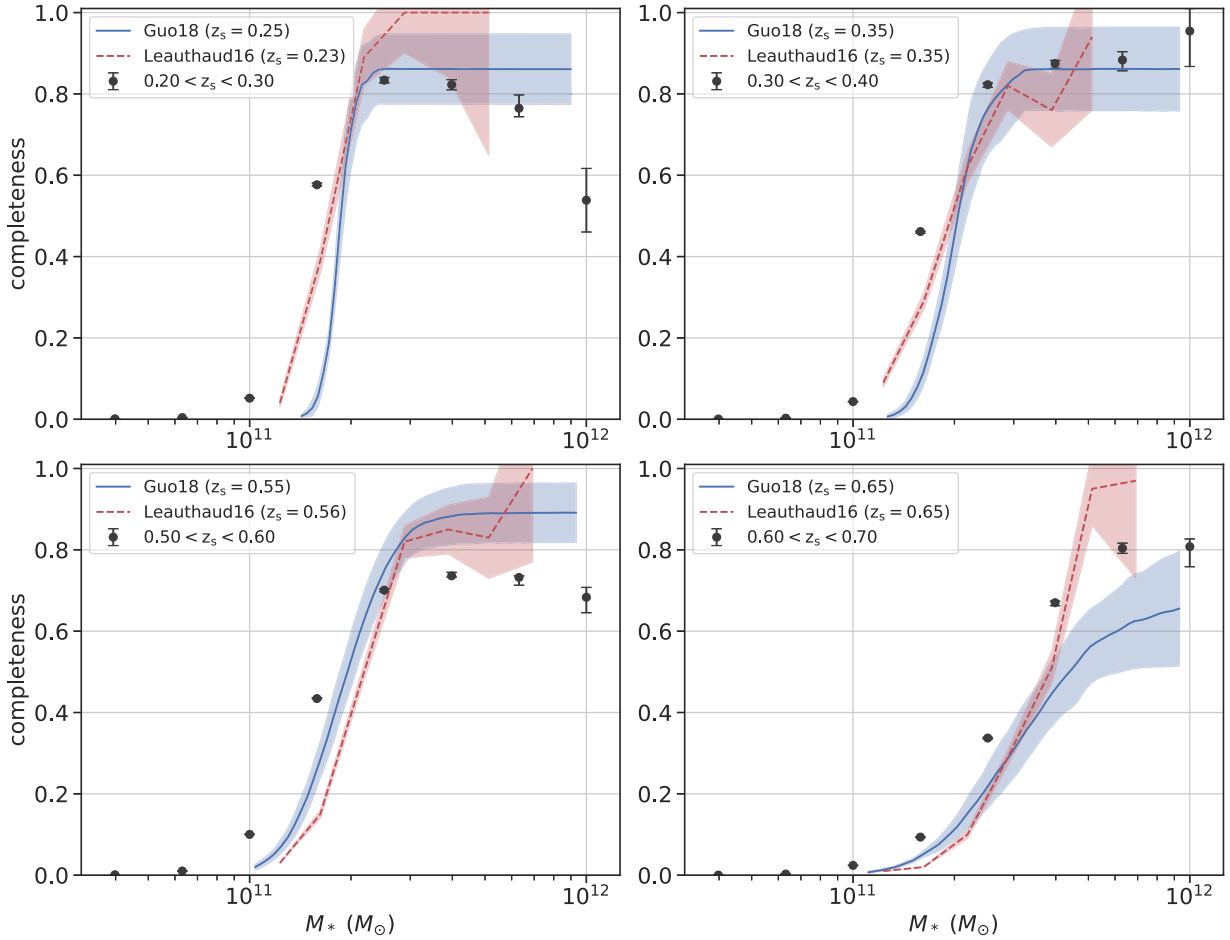

Figure 12. Stellar mass completeness, compared to the results from Leauthaud et al. (2016) and Guo et al. (2018).

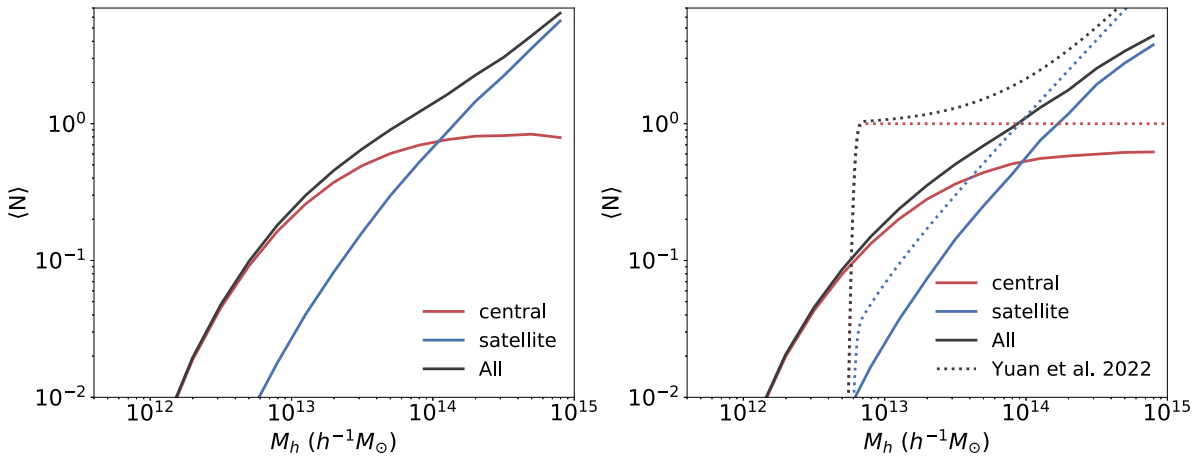

Figure 13. HODs of the LOWZ (left) and CMASS (right) samples, derived from our SHMRs, after taking the stellar mass completeness into account. The HOD of the CMASS sample from Yuan et al. (2022a) is also presented for comparison.

This publication has made use of data products from the Sloan Digital Sky Survey (SDSS). Funding for SDSS and SDSS II has been provided by the Alfred P. Sloan Foundation, the Participating Institutions, the National Science Foundation, the U.S. Department of Energy, the National Aeronautics and Space Administration, the Japanese Monbukagakusho, the Max Planck Society, and the Higher Education Funding Council for England.

Funding for SDSS III has been provided by the Alfred P. Sloan Foundation, the Participating Institutions, the National Science Foundation, and the U.S. Department of Energy Office of Science. The SDSS III website is http://www.sdss3.org/. SDSS III is managed by the Astrophysical Research Consortium for the Participating Institutions of the SDSS III Collaboration, including the University of Arizona, the Brazilian Participation Group, Brookhaven National

Laboratory, Carnegie Mellon University, the University of Florida, the French Participation Group, the German Participation Group, Harvard University, the Instituto de Astrofisica de Canarias, the Michigan State/Notre Dame/JINA Participation Group, Johns Hopkins University, Lawrence Berkeley National Laboratory, the Max Planck Institute for Astrophysics, the Max Planck Institute for Extraterrestrial Physics, New Mexico State University, New York University, Ohio State University, Pennsylvania State University, the University of Portsmouth, Princeton University, the Spanish Participation Group, the University of Tokyo, the University of Utah, Vanderbilt University, the University of Virginia, the University of Washington, and Yale University.

The Legacy Surveys consist of three individual and complementary projects: the Dark Energy Camera Legacy Survey (DECaLS; Proposal ID #2014B-0404; PIs: David Schlegel and Arjun Dey), the Beijing-Arizona Sky Survey (BASS; NOAO Prop. ID #2015A-0801; PIs: Zhou Xu and Xiaohui Fan), and the Mayall z-band Legacy Survey (MzLS; Prop. ID #2016A-0453; PI: Arjun Dey). DECaLS, BASS, and MzLS together include data obtained, respectively, at the Blanco telescope, Cerro Tololo Inter-American Observatory, NSF's NOIRLab; the Bok telescope, Steward Observatory, University of Arizona; and the Mayall telescope, Kitt Peak National Observatory, NOIRLab. The Legacy Surveys project is honored to be permitted to conduct astronomical research on Iolkam Duag (Kitt Peak), a mountain with particular significance to the Tohono Oodham Nation.

Appendix A
Verifying the Completeness

We verify our method of determining the mass limits by comparing the $\bar{n}_2 w_p$ measurements between $z_s < 0.2$ (four redshift bins) and $z_s < 0.15$ (three redshift bins) for $\mathrm{pop}_1 = 10^{11.2} M_\odot$ and $\mathrm{pop}_2 = 10^{8.6} M_\odot$. According to our results, for DECaLS, galaxies with $10^{8.6} M_\odot$ are exactly complete at $z_s = 0.2$, while galaxies with $10^{8.4} M_\odot$ are only complete at $z_s = 0.15$. If $10^{8.6} M_\odot$ is still not complete at $z_s = 0.2$, the measured $\bar{n}_2 w_p$ from $z_s < 0.2$ will be lower than that from $z_s < 0.15$. However, as shown in Figure A1, there is no systematic difference between the results from the two redshift ranges, verifying that $10^{8.6} M_\odot$ is complete at $z_s = 0.2$ for DECaLS.

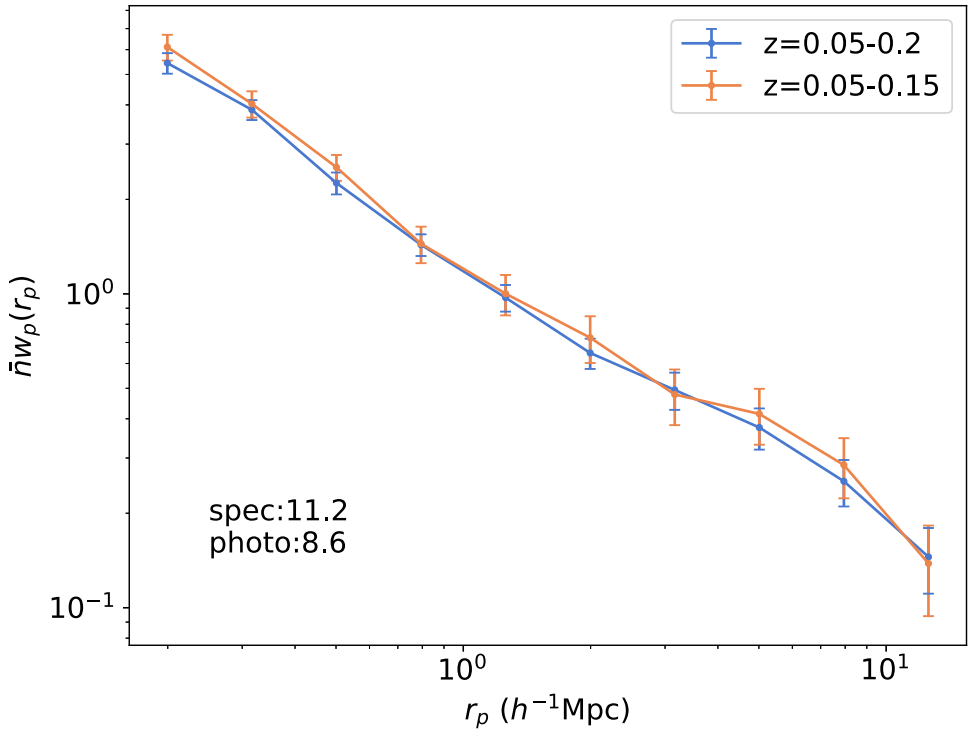

Figure A1. PAC measurements for $\mathrm{pop}_1 = 10^{11.2} M_\odot$ and $\mathrm{pop}_2 = 10^{8.6} M_\odot$ at $z_s < 0.2$ (blue) and $z_s < 0.15$ (orange).

Appendix B
Posterior Distributions of the Parameters

We show the posterior distributions for the parameters of the BP13 model at the Main, LOWZ, and CMASS redshift ranges in Figures B1, B2, and B3. The results of the DP model are also displayed in Figures B4, B5, and B6.

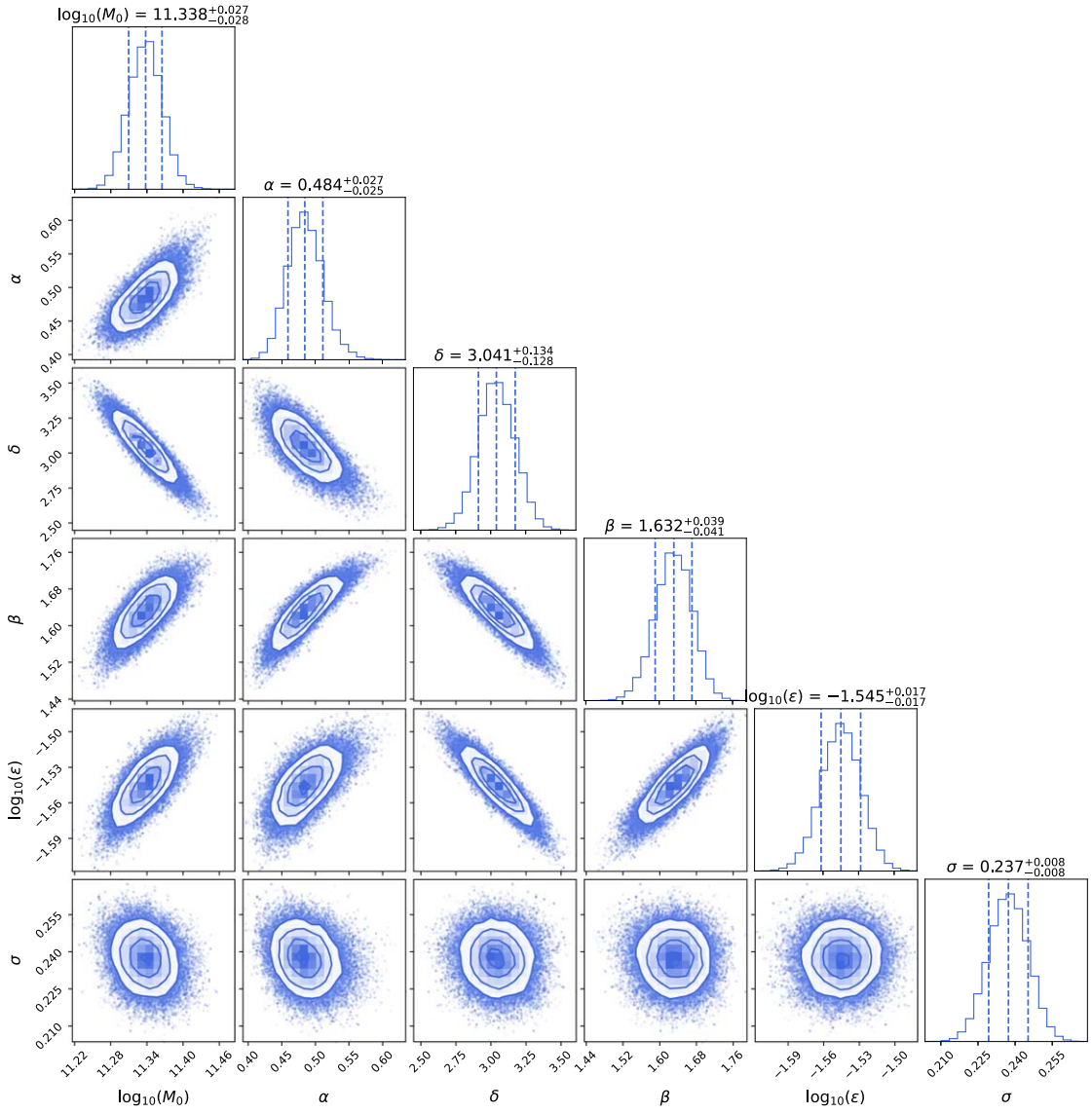

Figure B1. Posterior distributions of the parameters in the BP13 model in the Main sample redshift range ($z_s < 0.2$). The central value is a median, and the error means the 16th–84th percentiles, after the other parameters have been marginalized over.

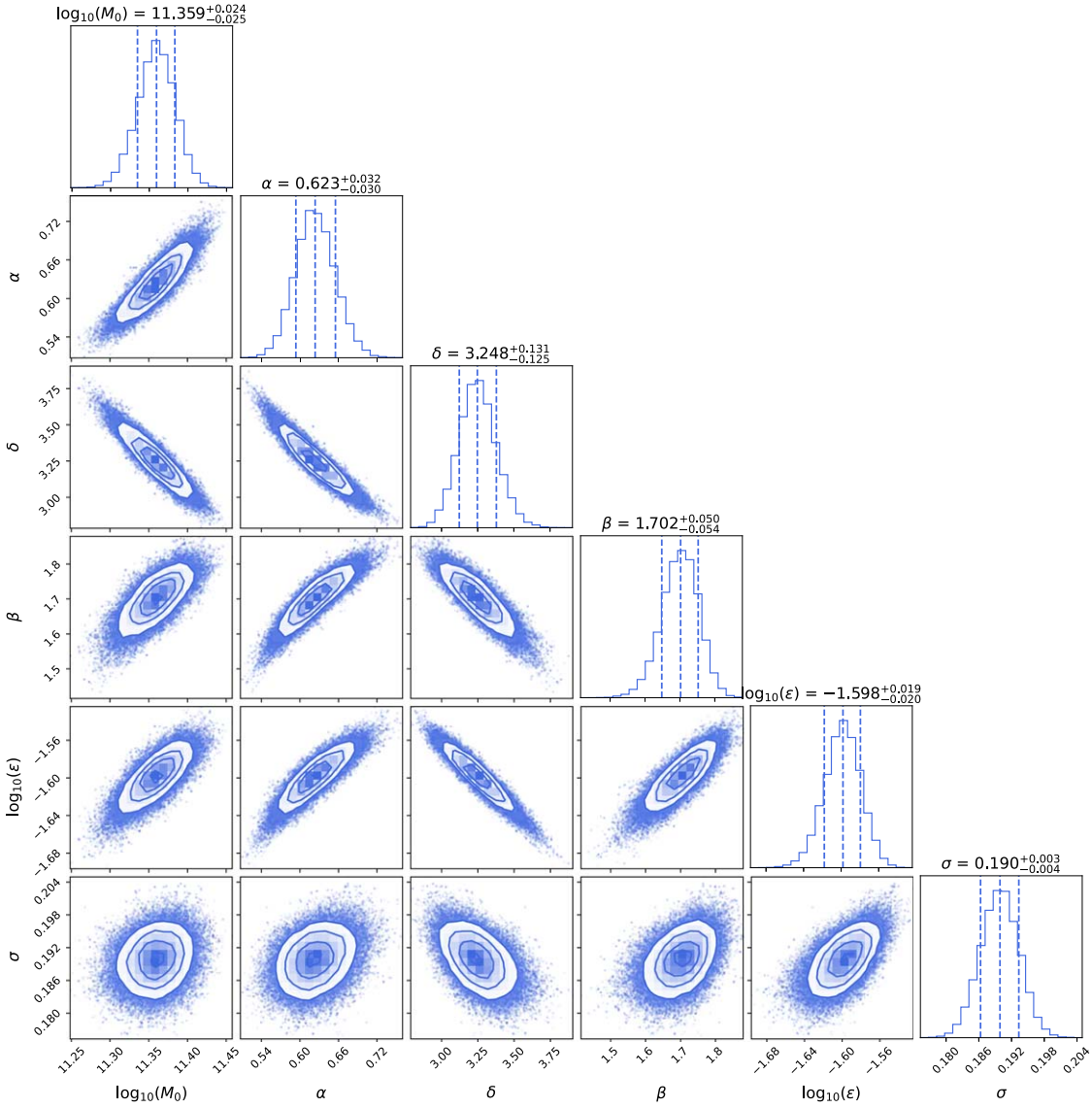

Figure B2. The same as Figure B1, but for the BP13 model in the LOWZ redshift range ($0.2 < z_s < 0.4$).

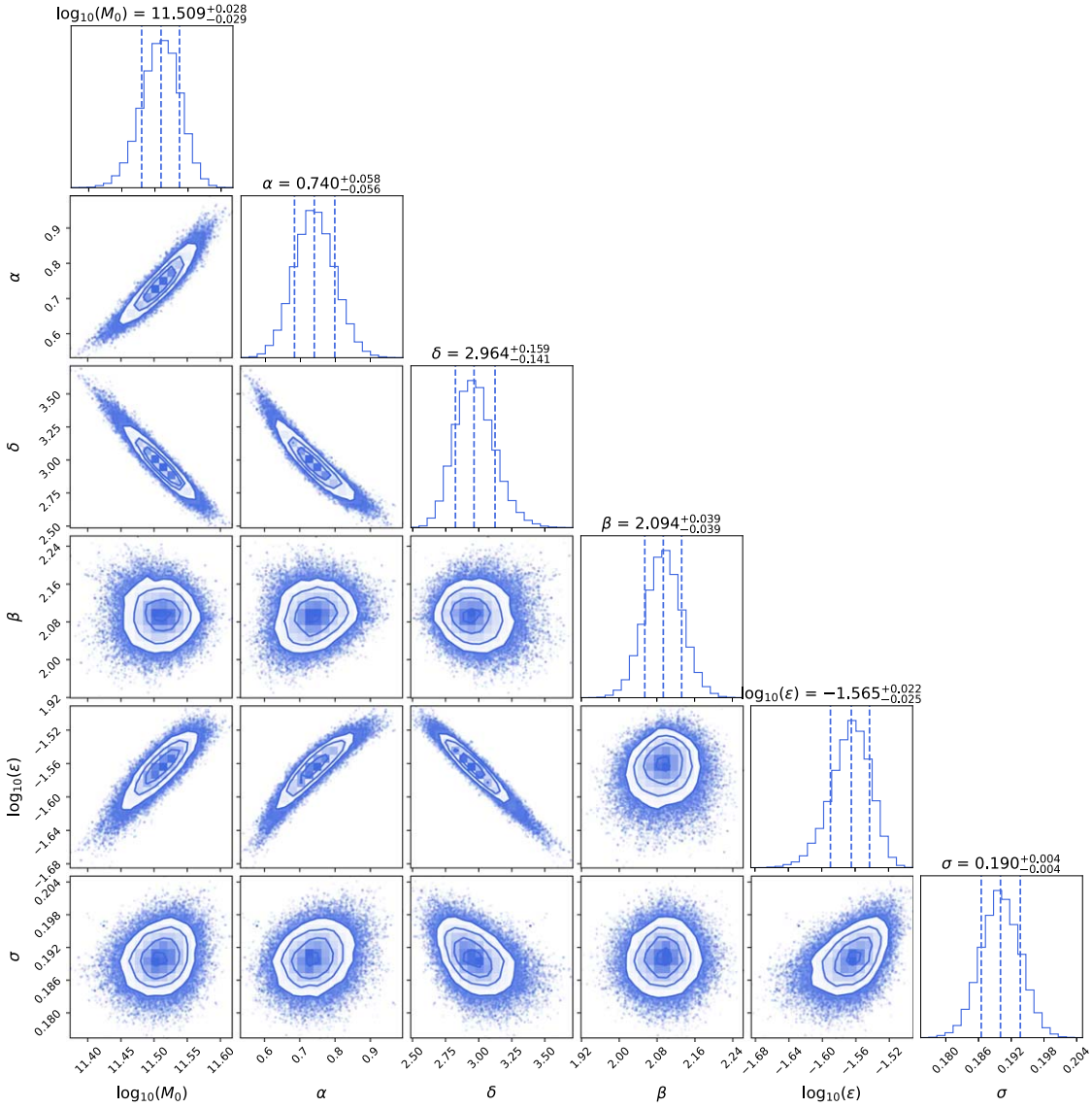

Figure B3. The same as Figure B1, but for the BP13 model in the CMASS redshift range ($0.5 < z_s < 0.7$).

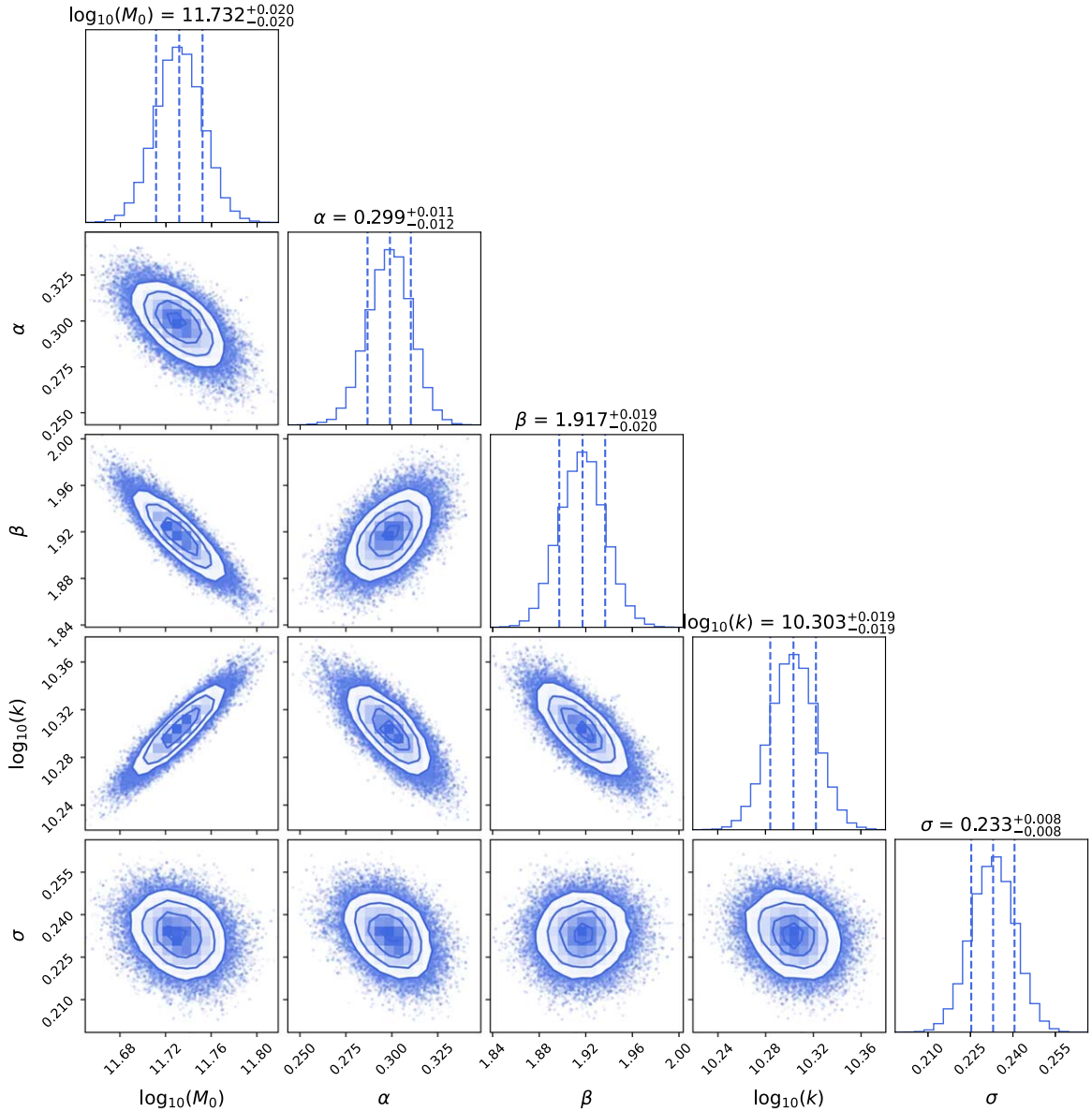

Figure B4. Posterior distributions of the parameters in the DP model in the Main sample redshift range ($z_s < 0.2$). The central value is a median, and the error means the 16th–84th percentiles, after the other parameters have been marginalized over.

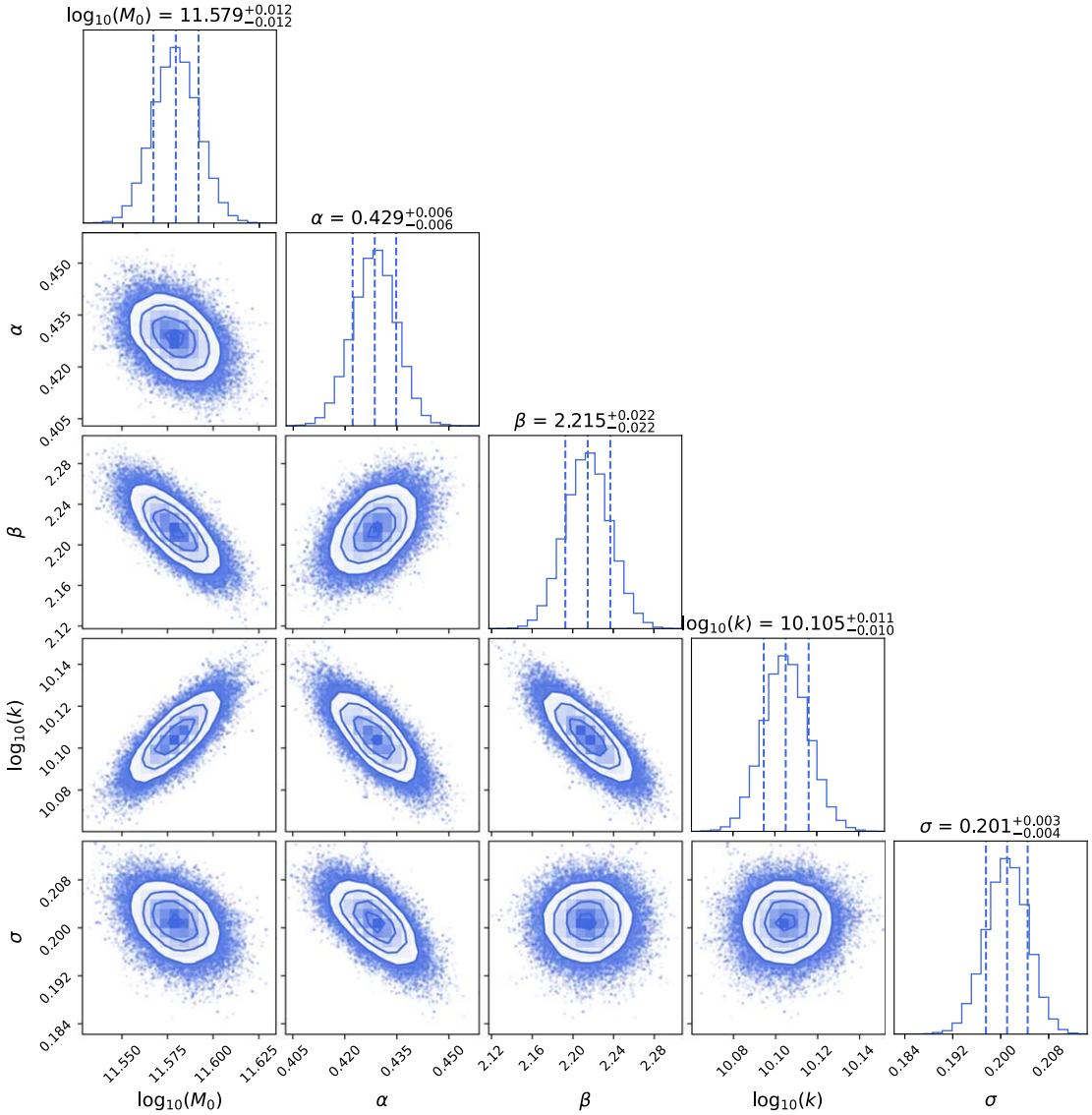

Figure B5. The same as Figure B4, but for the DP model in the LOWZ redshift range ($0.2 < z_s < 0.4$).

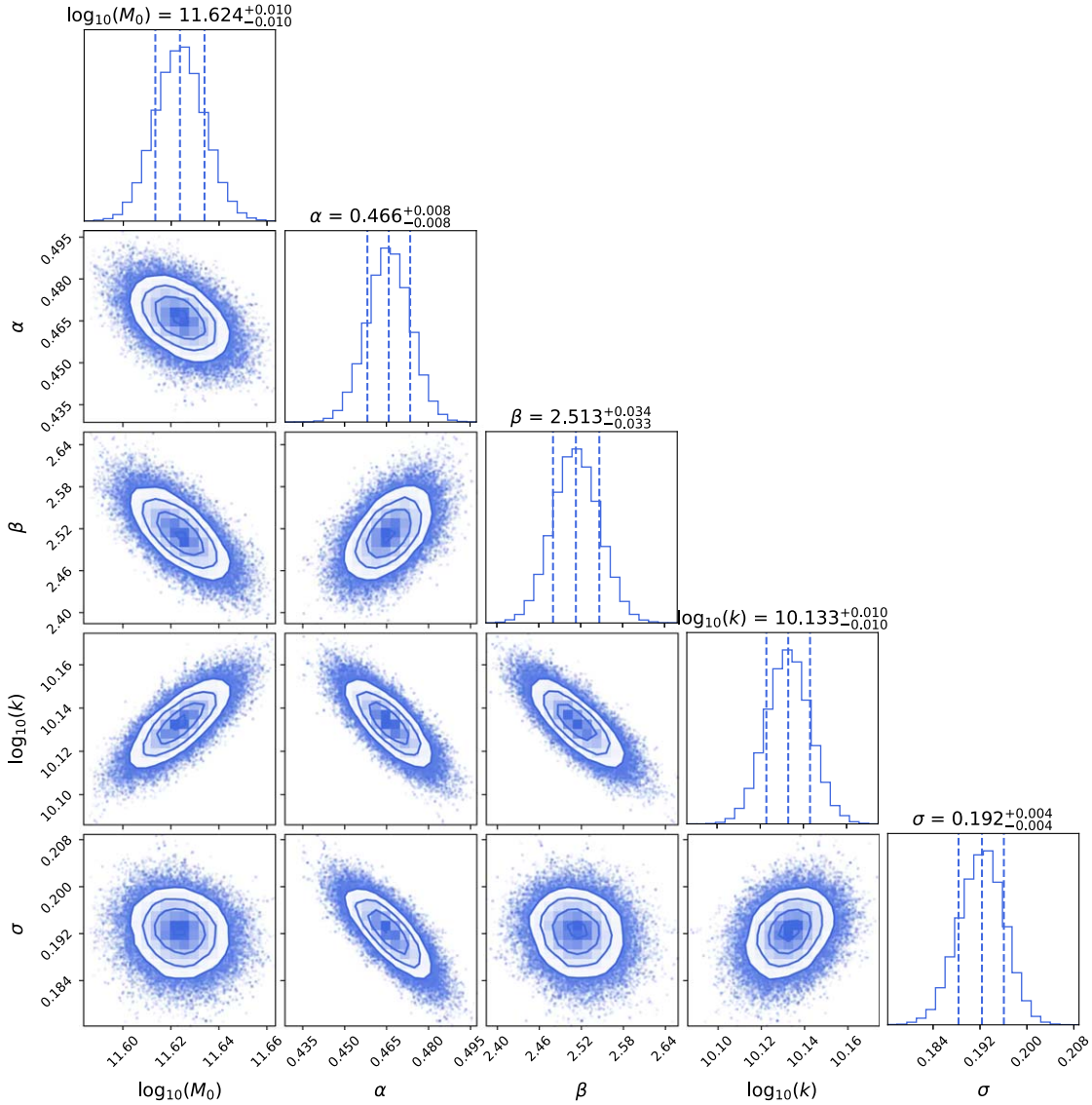

Figure B6. The same as Figure B4, but for the DP model in the CMASS redshift range ($0.5 < z_s < 0.7$).

Appendix C
The GSMFs from Abundance Matching in Tabular Form

In Table C1, we list the GSMFs inferred from our constrained BP13 abundance matching model for the three redshift ranges: $z_s < 0.2$, $0.2 < z_s < 0.4$, and $0.5 < z_s < 0.7$. The GSMFs are all constrained to subpercent levels.

Table C1
The GSMFs $\log_{10}(\Phi/\mathrm{Mpc}^{-3}\mathrm{dex}^{-1})$ at Different Redshifts from the BP13 Model

$\log_{10}(M_*/M_\odot)$	$z_s < 0.2$	$0.2 < z_s < 0.4$	$0.5 < z_s < 0.7$
8.0	$-1.227^{+0.012}_{-0.013}$		
8.2	$-1.310^{+0.012}_{-0.014}$		
8.4	$-1.412^{+0.010}_{-0.011}$		
8.6	$-1.524^{+0.008}_{-0.009}$		
8.8	$-1.642^{+0.009}_{-0.009}$		
9.0	$-1.758^{+0.009}_{-0.010}$		
9.2	$-1.863^{+0.008}_{-0.010}$	$-1.890^{+0.010}_{-0.008}$	
9.4	$-1.951^{+0.006}_{-0.009}$	$-1.973^{+0.009}_{-0.007}$	
9.6	$-2.022^{+0.006}_{-0.009}$	$-2.040^{+0.008}_{-0.005}$	
9.8	$-2.078^{+0.006}_{-0.010}$	$-2.096^{+0.008}_{-0.005}$	$-2.205^{+0.008}_{-0.008}$
10.0	$-2.124^{+0.007}_{-0.010}$	$-2.144^{+0.009}_{-0.006}$	$-2.243^{+0.007}_{-0.007}$
10.2	$-2.170^{+0.007}_{-0.010}$	$-2.195^{+0.009}_{-0.006}$	$-2.277^{+0.007}_{-0.006}$
10.4	$-2.232^{+0.007}_{-0.008}$	$-2.268^{+0.008}_{-0.007}$	$-2.324^{+0.007}_{-0.006}$
10.6	$-2.337^{+0.007}_{-0.007}$	$-2.389^{+0.008}_{-0.008}$	$-2.417^{+0.007}_{-0.007}$
10.8	$-2.513^{+0.009}_{-0.008}$	$-2.586^{+0.008}_{-0.008}$	$-2.592^{+0.007}_{-0.009}$
11.0	$-2.787^{+0.011}_{-0.010}$	$-2.878^{+0.009}_{-0.008}$	$-2.869^{+0.007}_{-0.009}$
11.2	$-3.177^{+0.012}_{-0.013}$	$-3.266^{+0.011}_{-0.008}$	$-3.247^{+0.008}_{-0.010}$
11.4	$-3.693^{+0.016}_{-0.020}$	$-3.751^{+0.013}_{-0.009}$	$-3.721^{+0.011}_{-0.011}$
11.6	$-4.347^{+0.026}_{-0.035}$	$-4.343^{+0.018}_{-0.014}$	$-4.291^{+0.019}_{-0.017}$
11.8		$-5.070^{+0.028}_{-0.025}$	$-4.979^{+0.037}_{-0.031}$

Appendix D
Stellar Mass Completeness of the LOWZ and CMASS Samples

In Table D1, we list the stellar mass completeness of the LOWZ and CMASS samples at different redshift ranges.

In Table D2, we simulate the target selection process of the CMASS sample, with $10^{11.8}M_\odot$ and $10^{12.0}M_\odot$, using the DECaLS photoz sample at $0.5 < z_p < 0.7$. Notice that the completeness accounts well for the results presented in Figure 12.

Table D1
Logarithmic ($\log_{10}$) Stellar Mass Completeness of the LOWZ and CMASS Samples at Different Redshift Ranges

z_s	$10^{10.6}M_\odot$ $10^{11.8}M_\odot$	$10^{10.8}M_\odot$ $10^{12.0}M_\odot$	$10^{11.0}M_\odot$	$10^{11.2}M_\odot$	$10^{11.4}M_\odot$	$10^{11.6}M_\odot$
0.20–0.40	-3.090 ± 0.014	-2.496 ± 0.008	-1.333 ± 0.003	-0.299 ± 0.002	-0.083 ± 0.003	-0.067 ± 0.004
	-0.076 ± 0.010	-0.086 ± 0.031				
0.20–0.25	-2.862 ± 0.029	-2.313 ± 0.016	-1.140 ± 0.006	-0.182 ± 0.003	-0.072 ± 0.005	-0.110 ± 0.010
	-0.132 ± 0.023	-0.697 ± 0.136				
0.25–0.30	-3.050 ± 0.028	-2.449 ± 0.015	-1.422 ± 0.008	-0.282 ± 0.003	-0.085 ± 0.005	-0.071 ± 0.008
	-0.092 ± 0.021	-0.099 ± 0.070				
0.30–0.35	-3.052 ± 0.024	-2.446 ± 0.014	-1.198 ± 0.005	-0.262 ± 0.003	-0.081 ± 0.004	-0.063 ± 0.007
	-0.079 ± 0.016	-0.059 ± 0.054				
0.35–0.40	-3.338 ± 0.029	-2.724 ± 0.020	-1.555 ± 0.006	-0.405 ± 0.003	-0.090 ± 0.003	-0.058 ± 0.007
	-0.038 ± 0.017	-0.001 ± 0.044				
0.50–0.70	-3.244 ± 0.010	-2.211 ± 0.003	-1.237 ± 0.002	-0.611 ± 0.001	-0.303 ± 0.002	-0.154 ± 0.003
	-0.114 ± 0.006	-0.132 ± 0.014				
0.50–0.55	-2.862 ± 0.012	-1.888 ± 0.007	-0.888 ± 0.002	-0.280 ± 0.002	-0.144 ± 0.003	-0.135 ± 0.005
	-0.158 ± 0.012	-0.196 ± 0.029				
0.55–0.60	-3.159 ± 0.017	-2.094 ± 0.007	-1.128 ± 0.003	-0.450 ± 0.002	-0.164 ± 0.003	-0.126 ± 0.005
	-0.117 ± 0.010	-0.142 ± 0.027				
0.60–0.65	-3.521 ± 0.025	-2.401 ± 0.008	-1.468 ± 0.004	-0.848 ± 0.003	-0.310 ± 0.003	-0.116 ± 0.004
	-0.089 ± 0.008	-0.126 ± 0.026				
0.65–0.70	-3.822 ± 0.033	-2.786 ± 0.013	-1.823 ± 0.006	-1.311 ± 0.005	-0.707 ± 0.004	-0.234 ± 0.005
	-0.094 ± 0.009	-0.074 ± 0.022				

Table D2
Numbers of Galaxies with $10^{11.8}M_{\odot}$ and $10^{12.0}M_{\odot}$ after Each Target Selection Step of CMASS, Using the DECaLS Photoz Sample at $0.5 < z_p < 0.7$

Steps	$10^{11.8}M_{\odot}$	$10^{12.0}M_{\odot}$
DECaLS	10824	1484
SDSS photometry matched	10467	1403
Low-z cut: $\lvert d_{\perp}\rvert > 0.55$[a]	10320	1375
Constant mass cut: $i_{\rm cmod} < 19.86 + 1.6(d_{\perp} - 0.8)$	10123	1364
Magnitude limit cut: $17.5 < i_{\rm cmod} < 19.9$	9953	1354
Problematic deblending cut: $r_{\rm mod} - i_{\rm mod} < 2$	9868	1340
Magnitude limit cut: $i_{\rm fib2} < 21.5$[b]	9655	1328
Star–galaxy separation: $i_{\rm psf} - i_{\rm mod} > 0.2 + 0.2(20.0 - i_{\rm mod})$	9637	1327
Star–galaxy separation: $z_{\rm psf} - z_{\rm mod} > 9.125 - 0.46z_{\rm mod}$	9581	1318
CMASS matched[c]	8598 (79%)	1123 (76%)

Notes.
[a] $|d_{\perp}| = (r_{\rm mod} - i_{\rm mod}) - (g_{\rm mod} - r_{\rm mod})/8$.
[b] $i_{\rm fib2}$ is the expected i-band magnitude through the SDSS III 2″ fibers.
[c] Since the footprint of the CMASS sample is slightly smaller than that of the SDSS photometric sample, the number is corrected using the area ratio.

ORCID iDs

Kun Xu https://orcid.org/0000-0002-7697-3306
Y. P. Jing https://orcid.org/0000-0002-4534-3125
Yun Zheng https://orcid.org/0000-0001-6575-0142

References

Abazajian, K. N., Adelman-McCarthy, J. K., Agüeros, M. A., et al. 2009, ApJS, 182, 543
Ahn, C. P., Alexandroff, R., Allende Prieto, C., et al. 2012, ApJS, 203, 21
Ahumada, R., Prieto, C. A., Almeida, A., et al. 2020, ApJS, 249, 3
Alam, S., Albareti, F. D., Allende Prieto, C., et al. 2015, ApJS, 219, 12
Baldry, I. K., Glazebrook, K., & Driver, S. P. 2008, MNRAS, 388, 945
Bartelmann, M., & Schneider, P. 2001, PhR, 340, 291
Behroozi, P. S., Wechsler, R. H., & Conroy, C. 2013, ApJ, 770, 57
Behroozi, P., Wechsler, R. H., Hearin, A. P., & Conroy, C. 2019, MNRAS, 488, 3143
Berlind, A. A., & Weinberg, D. H. 2002, ApJ, 575, 587
Bolton, A. S., Schlegel, D. J., Aubourg, É., et al. 2012, AJ, 144, 144
Boquien, M., Burgarella, D., Roehlly, Y., et al. 2019, A&A, 622, A103
Brammer, G. B., van Dokkum, P. G., & Coppi, P. 2008, ApJ, 686, 1503
Bruzual, G., & Charlot, S. 2003, MNRAS, 344, 1000
Bryan, G. L., & Norman, M. L. 1998, ApJ, 495, 80
Calzetti, D., Armus, L., Bohlin, R. C., et al. 2000, ApJ, 533, 682
Chabrier, G. 2003, PASP, 115, 763
Cole, S., Norberg, P., Baugh, C. M., et al. 2001, MNRAS, 326, 255
Colless, M., Dalton, G., Maddox, S., et al. 2001, MNRAS, 328, 1039
Dark Energy Survey Collaboration, Abbott, T., Abdalla, F. B., et al. 2016, MNRAS, 460, 1270
Davidzon, I., Bolzonella, M., Coupon, J., et al. 2013, A&A, 558, A23
Davidzon, I., Ilbert, O., Laigle, C., et al. 2017, A&A, 605, A70
Davis, M., Faber, S. M., Newman, J., et al. 2003, Proc. SPIE, 4834, 161
DESI Collaboration, Aghamousa, A., Aguilar, J., et al. 2016, arXiv:1611.00036
Dey, A., Schlegel, D. J., Lang, D., et al. 2019, AJ, 157, 168
Driver, S. P., Bellstedt, S., Robotham, A. S. G., et al. 2022, MNRAS, 513, 439
Fontana, A., Salimbeni, S., Grazian, A., et al. 2006, A&A, 459, 745
Foreman-Mackey, D. 2016, JOSS, 1, 24
Foreman-Mackey, D., Hogg, D. W., Lang, D., & Goodman, J. 2013, PASP, 125, 306
Frenk, C. S., & White, S. D. M. 2012, AnP, 524, 507
Gao, H., Jing, Y. P., Zheng, Y., & Xu, K. 2022, ApJ, 928, 10
Garilli, B., Guzzo, L., Scodeggio, M., et al. 2014, A&A, 562, A23
Guo, H., Yang, X., & Lu, Y. 2018, ApJ, 858, 30
Guo, Q., White, S., Li, C., & Boylan-Kolchin, M. 2010, MNRAS, 404, 1111
Han, J., Cole, S., Frenk, C. S., Benitez-Llambay, A., & Helly, J. 2018, MNRAS, 474, 604
Han, J., Jing, Y. P., Wang, H., & Wang, W. 2012, MNRAS, 427, 2437
Hartley, W. G., Choi, A., Amon, A., et al. 2022, MNRAS, 509, 3547
Hinshaw, G., Larson, D., Komatsu, E., et al. 2013, ApJS, 208, 19
Ilbert, O., McCracken, H. J., Le Fèvre, O., et al. 2013, A&A, 556, A55
Ivezić, Ž, Kahn, S. M., Tyson, J. A., et al. 2019, ApJ, 873, 111
Jiang, C. Y., Jing, Y. P., Faltenbacher, A., Lin, W. P., & Li, C. 2008, ApJ, 675, 1095
Jing, Y. 2019, SCPMA, 62, 19511
Jing, Y. P., Mo, H. J., & Börner, G. 1998, ApJ, 494, 1
Jing, Y. P., & Suto, Y. 2002, ApJ, 574, 538
Kaiser, N. 1987, MNRAS, 227, 1
Landy, S. D., & Szalay, A. S. 1993, ApJ, 412, 64
Lang, D., Hogg, D. W., & Mykytyn, D. 2016, The Tractor: Probabilistic Astronomical Source Detection and Measurement, Astrophysics Source Code Library, ascl:1604.008
Laureijs, R., Amiaux, J., Arduini, S., et al. 2011, arXiv:1110.3193
Le Fèvre, O., Vettolani, G., Garilli, B., et al. 2005, A&A, 439, 845
Leauthaud, A., Bundy, K., Saito, S., et al. 2016, MNRAS, 457, 4021
Leja, J., Speagle, J. S., Johnson, B. D., et al. 2020, ApJ, 893, 111
Li, C., Kauffmann, G., Jing, Y. P., et al. 2006, MNRAS, 368, 21
Li, C., & White, S. D. M. 2009, MNRAS, 398, 2177
Ma, C.-P., & Fry, J. N. 2000, ApJ, 543, 503
Maksimova, N. A., Garrison, L. H., Eisenstein, D. J., et al. 2021, MNRAS, 508, 4017
Marulli, F., Bolzonella, M., Branchini, E., et al. 2013, A&A, 557, A17
McLeod, D. J., McLure, R. J., Dunlop, J. S., et al. 2021, MNRAS, 503, 4413
Meneux, B., Guzzo, L., Garilli, B., et al. 2008, A&A, 478, 299
Mo, H., van den Bosch, F. C., & White, S. 2010, Galaxy Formation and Evolution (Cambridge: Cambridge Univ. Press)
Mortlock, A., Conselice, C. J., Hartley, W. G., et al. 2015, MNRAS, 447, 2
Mostek, N., Coil, A. L., Cooper, M., et al. 2013, ApJ, 767, 89
Moster, B. P., Naab, T., & White, S. D. M. 2013, MNRAS, 428, 3121
Moster, B. P., Naab, T., & White, S. D. M. 2018, MNRAS, 477, 1822
Muzzin, A., Marchesini, D., Stefanon, M., et al. 2013, ApJ, 777, 18
Naab, T., & Ostriker, J. P. 2017, ARA&A, 55, 59
Norberg, P., Baugh, C. M., Hawkins, E., et al. 2002, MNRAS, 332, 827
Peacock, J. A., & Smith, R. E. 2000, MNRAS, 318, 1144
Pozzetti, L., Bolzonella, M., Lamareille, F., et al. 2007, A&A, 474, 443
Reid, B., Ho, S., Padmanabhan, N., et al. 2016, MNRAS, 455, 1553
Schlegel, D. J., Finkbeiner, D. P., & Davis, M. 1998, ApJ, 500, 525
Scoccimarro, R. 2004, PhRvD, 70, 083007
Seljak, U. 2000, MNRAS, 318, 203
Shuntov, M., McCracken, H. J., Gavazzi, R., et al. 2022, A&A, 664, A61
Somerville, R. S., & Davé, R. 2015, ARA&A, 53, 51
Steidel, C. C., Adelberger, K. L., Shapley, A. E., et al. 2003, ApJ, 592, 728
Takada, M., Ellis, R. S., Chiba, M., et al. 2014, PASJ, 66, R1
Tomczak, A. R., Quadri, R. F., Tran, K.-V. H., et al. 2014, ApJ, 783, 85
Treu, T. 2010, ARA&A, 48, 87
Wang, L., & Jing, Y. P. 2010, MNRAS, 402, 1796
Wang, W., Jing, Y. P., Li, C., Okumura, T., & Han, J. 2011, ApJ, 734, 88
Wechsler, R. H., & Tinker, J. L. 2018, ARA&A, 56, 435
Wright, A. H., Driver, S. P., & Robotham, A. S. G. 2018, MNRAS, 480, 3491
Wright, E. L., Eisenhardt, P. R. M., Mainzer, A. K., et al. 2010, AJ, 140, 1868
Xu, K., Jing, Y. P., & Gao, H. 2022a, ApJ, 939, 104
Xu, K., Zheng, Y., & Jing, Y. 2022b, ApJ, 925, 31
Yang, X., Mo, H. J., & van den Bosch, F. C. 2003, MNRAS, 339, 1057
Yang, X., Mo, H. J., & van den Bosch, F. C. 2009, ApJ, 695, 900
Yang, X., Mo, H. J., van den Bosch, F. C., Zhang, Y., & Han, J. 2012, ApJ, 752, 41
York, D. G., Adelman, J., Anderson, J. E. J., et al. 2000, AJ, 120, 1579
Yuan, S., Garrison, L. H., Eisenstein, D. J., & Wechsler, R. H. 2022a, MNRAS, 515, 871
Yuan, S., Garrison, L. H., Hadzhiyska, B., Bose, S., & Eisenstein, D. J. 2022b, MNRAS, 510, 3301
Zheng, Z., Coil, A. L., & Zehavi, I. 2007, ApJ, 667, 760
Zheng, Z., & Guo, H. 2016, MNRAS, 458, 4015
Zheng, Z., Berlind, A. A., Weinberg, D. H., et al. 2005, ApJ, 633, 791
Zhou, R., Newman, J. A., Mao, Y.-Y., et al. 2021, MNRAS, 501, 3309
Zu, Y., & Mandelbaum, R. 2015, MNRAS, 454, 1161